3.46 Ga Apex chert ‘microfossils’ reinterpreted as mineral artefacts produced during phyllosilicate exfoliation

David Wacey, Martin Saunders, Charlie Kong, Alexander Brasier, Martin Brasier

PII: S1342-937X(15)00190-2
DOI: doi: 10.1016/j.gr.2015.07.010
Reference: GR 1485

To appear in: *Gondwana Research*

Received date: 30 April 2015
Revised date: 15 July 2015
Accepted date: 26 July 2015

Please cite this article as: Wacey, David, Saunders, Martin, Kong, Charlie, Brasier, Alexander, Brasier, Martin, 3.46 Ga Apex chert ‘microfossils’ reinterpreted as mineral artefacts produced during phyllosilicate exfoliation, *Gondwana Research* (2015), doi: 10.1016/j.gr.2015.07.010

3.46 Ga Apex chert 'microfossils' reinterpreted as mineral artefacts produced during phyllosilicate exfoliation

David Wacey[a,b,1], Martin Saunders[c], Charlie Kong[d], Alexander Brasier[e], and Martin Brasier[f†]

[a]*School of Earth Sciences, University of Bristol, Queen's Road, Bristol, BS8 1RJ, UK.*
[b]*Australian Research Council Centre of Excellence for Core to Crust Fluid Systems, & Centre for Microscopy Characterisation and Analysis, The University of Western Australia, 35 Stirling Highway, Crawley, WA 6009, Australia.*
[c]*Centre for Microscopy Characterisation and Analysis, The University of Western Australia, 35 Stirling Highway, Crawley, WA 6009, Australia.*
[d] *Electron Microscopy Unit, University of New South Wales, Kingsford, NSW 2052, Australia*
[e] *School of Geosciences, Meston Building, University of Aberdeen, Old Aberdeen, AB24 3UE, UK*
[f†]*Department of Earth Sciences, University of Oxford, South Parks Road, Oxford, OX1 3AN, UK.*

[1]Corresponding Author:
David Wacey
School of Earth Sciences
University of Bristol
Life Sciences Building
24 Tyndall Avenue
Bristol, BS8 1TQ
Email: David.Wacey@bristol.ac.uk
Tel: 0117 954 5400
Fax: 0117 954 5420

ABSTRACT

Filamentous microstructures from the 3.46 billion year (Ga)-old Apex chert of Western Australia have been interpreted as remnants of Earth's oldest cellular life, but their purported biological nature has been robustly questioned on numerous occasions. Despite recent claims to the contrary, the controversy surrounding these famous microstructures remains unresolved.

Here we interrogate new material from the original 'microfossil site' using high spatial resolution electron microscopy to decode the detailed morphology and chemistry of the Apex filaments. Light microscopy shows that our newly discovered filaments are identical to the previously described 'microfossil' holotypes and paratypes. Scanning and transmission electron microscopy data show that the filaments comprise chains of potassium- and barium-rich phyllosilicates, interleaved with carbon, minor quartz and iron oxides. Morphological features previously cited as evidence for cell compartments and dividing cells are shown to be carbon-coated stacks of phyllosilicate crystals. Three-dimensional filament reconstructions reveal non-rounded cross sections and examples of branching incompatible with a filamentous prokaryotic origin for these structures.

When examined at the nano-scale, the Apex filaments exhibit no biological morphology nor bear any resemblance to younger *bona fide* carbonaceous microfossils. Instead, available evidence indicates that the microstructures formed during fluid-flow events that facilitated the hydration, heating and

exfoliation of potassium mica flakes, plus the redistribution and adsorption of barium, iron and carbon within an active hydrothermal system.

Keywords: Apex Chert, Pilbara Craton, Microfossils, Pseudofossils, Archean Life

1. Introduction

The Apex microfossil debate is one of the longest running and highest profile controversies in palaeobiology and evolution. At its heart are filamentous microstructures found in black chert veins within the 3.46 Ga Apex Basalt near Marble Bar in the Pilbara Craton of Western Australia (Schopf and Packer, 1987; Schopf, 1993). On one side of the debate is the claim that these microstructures represent at least eleven species of filamentous prokaryote microfossils comprising some of the earliest morphological evidence of life on Earth (Schopf and Packer, 1987; Schopf, 1992, 1993, 1999, 2006; Schopf et al., 2007; Schopf and Kudryavtsev 2009, 2012). An opposing view is that these microstructures are not microfossils, merely blobs of carbon, fortuitously arranged in roughly filamentous patterns around crystal boundaries (Brasier et al., 2002, 2004, 2005, 2006, 2011, 2015). Adding complexity to the debate are separate reports from elsewhere in the Apex chert of other non-biological microfossil-like artefacts and later carbonaceous contaminants (Pinti et al., 2009; Marshall et al., 2011; Olcott Marshall et al., 2012; Sforna et al., 2014), inconclusive chemical studies attempting to assess the biogenictiy of Apex chert carbon (De Gregorio and Sharp, 2006; De Gregorio et al., 2009), plus questions over the suitability of the confocal laser Raman microspectroscopy technique favoured by the proponents of a biological origin (Pasteris and Wopenka, 2002, 2003; Marshall and Olcott Marshall, 2013). Below we summarise the history of the study of the Apex chert microstructures before presenting our new high spatial resolution electron microscopy data.

1.1. History of the Apex microfossil debate

The Apex chert 'microfossils' first entered the literature in 1987 (Schopf and Packer, 1987) and were described in detail in the early 1990's (Schopf, 1992, 1993). They were formally classified as fossils of uncertain biological affinity, 'Bacteria *Incertae Sedis*'. However, phrases in Schopf (1993) such as 'I interpret…..the remaining seven species….as probable cyanobacteria' and '…suggest that cyanobacterial oxygen-producing photosynthesizers may already have been extant this early in Earth history' heavily implied a cyanobacterial affinity. This implication entered into many textbooks and popular science books written in subsequent years. With it came the inference of a relatively advanced level of prokaryote evolution at 3.5 Ga, plus an early origin of photosynthetic oxygen production on Earth. Little attempt was made to test these ~~dogmatic~~ assumptions until the authenticity of the 'microfossils' themselves was challenged almost a decade later (Dalton, 2002).

There were a number of subtle details in the initial reports (Schopf and Packer, 1987; Schopf, 1992, 1993) that are not wholly consistent with an interpretation of the filaments as microfossils, yet a decade or more passed without a thorough re-examination of the type material. Firstly, the claimed taxonomic diversity is particularly vast, being more diverse than 92% of all other Precambrian filamentous fossil assemblages. Comparable diversity is not seen until some 1500 Ma later, for example in the Gunflint Formation of Canada (Barghoorn and Tyler, 1965). Such taxonomic diversity in a deposit of this great age would require an early origin and diversification, then very slow evolution, of filamentous microbes. A number of the figured microfossils are rather light in colour, with yellow, orange and light brown examples (see colour images in Brasier et al., 2011). This is in contrast to other reports of early Archean carbon that illustrate a dark brown to black colour, and hence raises questions about the true age and carbonaceous composition of some of the Apex microstructures. The filaments do not exhibit biological behaviour; instead they are solitary, irregular and randomly orientated. Questions were also raised about the selectivity of the data chosen for publication, with suggestions that more complex objects exhibiting branching, a trait that would not have occurred in such primitive organisms, were withheld from publication (Packer quoted in Dalton, 2002). Although reported as ‘thin-sections’ (Schopf and Packer, 1987; Schopf 1993), the thicknesses of the rock slices containing the type specimens are not standard (30 µm) but range from 193 to 380 µm (Brasier et al., 2005). The structures illustrated by Schopf and Packer (1987) and Schopf (1993) cannot be imaged in a single depth plain: this requires montaging of several photographs. Inconsistencies between illustrations of the same specimens also occur (Schopf and Packer, 1987; Schopf, 1993); for example, Fig. 3i from Schopf (1993) is the same specimen as Fig. 1a from Schopf and Packer (1987) but the former omits what appears to be a fold in the filament seen in the top right of the latter.

In 2002, the Apex debate gathered pace with the publication of back-to-back papers in Nature (Brasier et al., 2002; Schopf et al., 2002). Brasier et al. (2002) presented new geological mapping data, a petrographic re-examination of the type material and observations from additional material collected from the original ‘microfossil’ locality. This revealed further inconsistencies in the earlier reports. For example, it had been claimed that the microfossils occurred in a sedimentary bedded chert unit and that all of the microfossils occurred in early rounded sedimentary clasts (Schopf, 1993). In contrast, Brasier et al. (2002) showed that the microstructures occurred in black chert veins that intrude the lower part of the Apex Basalt. Furthermore, Brasier et al. (2002) showed that the microstructures co-occurred with a suite of minerals and textures characteristic of a hydrothermal setting, and that near-identical micro-structures also occurred in later generations of chert matrix as well as other rock types in the immediate vicinity of the black chert veins. Using a computer-assisted montage imaging approach, Brasier et al. (2002) also showed that parts of the type microstructures had been left out of the original manually-montaged photomicrographs (Schopf and Packer, 1987; Schopf, 1993). This additional information appeared to show filament branching and distribution of carbon around ghosts of mineral crystals. The combined evidence led Brasier et al. (2002) to conclude that the ‘microfossils’ were in fact carbonaceous mineral rims that formed around recrystallizing grain margins during a complex series of hydrothermal events.

Schopf et al. (2002) dismissed the petrographic contextual arguments presented by Brasier et al. (2002). They countered with confocal laser Raman microspectroscopic data that demonstrated a kerogenous carbonaceous composition for the microfossils. These authors claimed that correlation of this kerogenous chemistry with morphologically identifiable features characteristic of microorganisms confirmed their earlier conclusion that the Apex microstructures were *bona fide* microfossils. Laser Raman specialists, however, felt that Schopf et al. (2002) had over-interpreted the data and went on to demonstrate that laser Raman cannot unambiguously distinguish carbon of a biological precursor from that of an abiotic nature (Pasteris and Wopenka, 2002, 2003). Since these seminal papers, the debate has swung back and forth with Schopf and colleagues using laser Raman and confocal laser scanning microscopy (CLSM) in an attempt to reassert the biogenicity of the microfossils (e.g., Schopf, 2006; Schopf et al., 2007; Schopf and Kudryavtsev 2009, 2012), while Brasier and colleagues have presented more detailed geological mapping and petrography in support of their mineral rim pseudofossil hypothesis (e.g., Brasier et al., 2004, 2005, 2006, 2011). Schopf and colleagues now concede that the geological setting is hydrothermal rather than sedimentary and have moved away from a cyanobacterial interpretation for the 'microfossils', suggesting instead that the 'microfossils' likely represent 'remnants of thermophilic microbes, preserved *in situ* and perhaps permineralized in hydrothermally milled and rounded organic rich clasts' (Schopf and Kudryavtsev, 2012).

In latter years the debate has been blurred somewhat by descriptions of further suites of abiogenic microfossil-like objects from various parts of the Apex chert (Pinti et al., 2009; Marshall et al., 2011), and a multitude of chemical analyses of Apex carbon (De Gregorio and Sharp, 2006; De Gregorio et al. 2009; Olcott Marshall et al., 2012; Sforna et al., 2014). There is no doubt that these studies have provided valuable data concerning the formation and subsequent alteration environments of the Apex chert and the carbon contained within. However, these microfossil-like artefacts do not show close similarity to the type Apex 'microfossils', and the chemical analyses were not performed on the 'microfossils'. This has led some to question their relevance to the (re)interpretation of the type Apex 'microfossils' (Schopf and Kudryavtsev, 2012) and, if anything, has made the original claims easier to defend. Indeed recently, Schopf and Kudryavtsev (2012) claimed 'a resolution of the controversy' in favour of a *bona fide* microfossil origin for the Apex chert microstructures, although no additional data to support this hypothesis was presented in that paper. However, it is clear that the controversy has not been resolved, highlighted by the vigorous debate that immediately followed publication of that paper (Marshall and Olcott Marshall, 2013; Olcott Marshall and Marshall, 2013; Pinti et al., 2013; Schopf and Kudryavtsev, 2013).

Here we return to the original microfossil locality and use high spatial resolution electron microscopy to show precisely what minerals and textures comprise filamentous microstructures equivalent to the 'microfossil' holotypes and paratypes. This allows us to demonstrate that the purported microfossil filaments are not cellular in nature and do not constitute morphologically preserved prokaryotes. Instead, they comprise sheets of phyllosilicates with carbon sandwiched in between. Our hypothesis of a phyllosilicate origin for the Apex 'microfossils' was first presented in Brasier et al. (2015) and this was supported by a subset of the data reported here. This contribution greatly expands on the evidence presented in Brasier et al. (2015) with analyses of many more filaments, plus three-dimensional data and comparative Raman data not previously published.

2. Materials and methods

2.1. Sample locality and geological setting

The c. 3.46 Ga Apex Basalt is found in the East Pilbara granite greenstone terrane of the Pilbara craton, Western Australia (Fig. 1). It is part of the Warrawoona Group, a 10-15 km thick volcano-sedimentary succession dominated by extrusive volcanic rocks with minor interstratified chert, barite, carbonate and volcaniclastic units. The ‘microfossils’ were initially reported from the Apex chert (informal name), the lowermost of several thin stratiform chert horizons within the Apex Basalt in the vicinity of Chinaman Creek, approximately 5 km west of the township of Marble Bar (Schopf and Packer, 1987; Schopf, 1993). However, the geological setting of the Apex ‘microfossils’ has been reinvestigated, with the results presented in detail in Brasier et al. (2005) and Brasier et al. (2011). In summary, this new geological mapping has shown that the ‘microfossils’ do not come from a sedimentary stratiform chert layer as initially claimed (Schopf, 1993) but from a hydrothermally influenced subsurface vein system, some 100 m below the stratiform Apex chert (Fig. 1c-d). This context has been supported by subsequent independent studies (Van Kranendonk, 2006; Pinti et al., 2009) and a hydrothermal geological context for the ‘microfossils’ is now widely accepted (Schopf and Kudryavtsev, 2012). The reinterpreted geological setting does not rule out the presence of life in these rocks because microorganisms are common in modern hydrothermal environments (e.g., Jannasch and Wirsen, 1981). It does, however, bring added complexity to the interpretation of any microstructures contained within such rocks, not least because of the possibility of the presence of abiogenic carbon generation in hydrothermal environments (e.g., Berndt et al., 1996) and the ease with which elements and minerals can be altered and transported by hydrothermal fluids.

The material studied here (sample CHIN-3) comes from the original ‘microfossil’ locality (Fig. 1c-d) and was collected in 2001 (see also locality CC4 of Brasier et al., 2011). Analysis of previously published type specimens is compromised by the 193-380 μm thick preparations (Brasier et al., 2005) making optical petrography difficult. There is also an understandable prohibition (by the Natural History Museum, London) on destructive or intrusive techniques, meaning for example that high spatial resolution approaches such as focused ion beam milling combined with scanning- or transmission-electron microscopy (FIB-SEM and FIB-TEM) cannot be performed on the type specimens. Our materials are therefore standard (~30 μm thick) polished geological thin sections, making optical characterisation more straightforward and allowing the application of the full range of high spatial resolution analytical techniques currently available to us. Crucially, filamentous microstructures found in our new material are identical to those found in the type material (see Section 3.1. for details), unlike some recent studies of the Apex chert (Pinti et al., 2009; Marshall et al., 2011).

2.2. Focussed ion beam (FIB) preparation of TEM samples

Prior to FIB milling the thin sections were examined by optical microscopy, 2D and 3D laser Raman plus SEM to gain an understanding of the filament distributions and morphologies, and to select the most appropriate targets for detailed study. Any risk of surface contamination leading to microfossil-like artefacts (for example during thin section preparation and polishing) are here mitigated because FIB preparation of TEM sections allows features below the surface (typically up to about 15 μm depth) of the thin sections to be targeted. The preliminary SEM work was performed using a *Zeiss Supra 1555* and the optical microscopy was performed using *Nikon Optiophot-2*, Nikon *Optiophot-pol* and *Zeiss Axioskop 2* microscopes.

Most TEM samples were prepared using a dual-beam FIB system (*FEI Nova NanoLab*) at the Electron Microscopy Unit (EMU), University of New South Wales. Electron beam imaging was used to identify microstructures of interest in the polished thin sections coated with c. 30 nm of gold, allowing site-specific TEM samples to be prepared. The TEM sections were prepared by a series of steps involving different Ga^+ ion beam energies and currents (see Wacey et al., 2012), resulting in ultrathin wafers of c. 100 nm thickness. These TEM wafers were extracted using an *ex-situ* micromanipulator and deposited on continuous-carbon copper TEM grids. One TEM wafer was prepared at the FEI factory in Brno, Czech Republic, using a dual-beam *FEI Helios NanoLab G3* instrument. Here, the partially thinned wafer was attached to an *Omniprobe®* copper TEM holder using platinum connector strips, then final thinning to c.80 nm was performed *in situ* on the holder. This protocol means that there is no carbon film underneath the wafer, simplifying subsequent carbon elemental mapping in the TEM.

2.3. TEM analysis of FIB-milled wafers

TEM data were obtained using a *FEI Titan G2 80-200* TEM/STEM with *ChemiSTEM Technology* operating at 200 kV, plus a *JEOL 2100* LaB_6 TEM operating at 200 kV equipped with a *Gatan Orius* CCD camera and *Tridiem* energy filter. Both instruments are located in the Centre for Microscopy, Characterisation and Analysis (CMCA) at The University of Western Australia. HAADF (high angle annular dark-field) STEM images and EDS (*ChemiSTEM*) maps were obtained on the *FEI Titan*. Energy filtered (EFTEM) elemental maps were obtained on the *JEOL 2100* using the conventional three-window technique (Brydson, 2001), with energy windows selected to provide optimum signal-to-noise. Selected area electron diffraction for mineral identification was performed on the *Jeol 2100* with an aperture that selected a ~200 nm field of view.

2.4. FIB-SEM and FIB-SEM 3D nano-tomography

FIB milling and SEM imaging was performed on a *Zeiss Auriga Crossbeam* dual beam instrument at EMU. The protocol was a modified version of that described in Wacey et al (2012), with milling and imaging parameters optimized to suit the type of sample (i.e. carbon, iron oxides and phyllosilicates within a silica matrix). Regions of interest (ROI) previously identified using optical microscopy and laser Raman micro-spectroscopy were covered with a protective (c. 1μm-thick) platinum layer. Initial front and side trenches were milled with a 10 nA Ga^+ ion beam. An additional gold coat was then applied and the sample was heated in an oven at ~50 °C overnight to minimize any instability caused by moisture escape/degassing during the opening of the trenches. The front face of the ROI was then cleaned and polished using a 2 nA beam current. Imaging was performed at 5 kV using the back-scattered electron (BSE) detector in order to minimise charging effects and maximise the contrast between minerals of differing masses. Sequential slices were milled with a 2 nA Ga^+ beam current and the slice spacing was 200 nm. The working distance (5.0 mm) was tracked during sequential imaging, and tilt correction was enabled. Each newly milled face was imaged (2048 x 1536 pixels) with an image capture time of ~80 seconds. This long image capture time was required to obtain images of high enough quality for subsequent 3D reconstruction. Semi quantitative elemental mapping of FIB-milled faces was performed using an *Oxford X-max SDD* energy dispersive X-ray spectroscopy (EDS) system attached to the *Zeiss Auriga Crossbeam* instrument, with detection limits of about 0.5-1 atomic %. Note that any technique involving a focused ion beam is destructive and could not be applied to the type specimens held at the Natural History Museum, London.

2.5. 3D reconstruction and visualisation

Sequential FIB-SEM nano-tomography images were stacked, aligned and cropped using *SPIERSalign* (Sutton et al., 2012). The resultant stacks were imported into the *AVIZO 8.0* software package where carbonaceous material was segmented allowing 3D models of the carbon associated with the filaments to be produced. The models were visualised and rendered in *AVIZO 8.0* and publication quality images were captured from multiple orientations in 3D space.

FIB-SEM nano-tomography collects mostly morphological data. The carbonaceous material studied here is easy to detect in SEM images because of its different mass (hence contrast/brightness) compared to the silicates and silica matrix in which it is found. In our source SEM backscatter electron images, for example, carbon appears black, silica and phyllosilicates grey, and iron oxides bright white; hence carbon can easily be segmented from the remaining material. We performed EDS chemical analysis on selected SEM slices to confirm that the chemistry matched with the morphological features we saw, but did not do EDS on every slice because that would have been impractical in terms of analysis time. Hence, the 3D reconstructions do not depend on the size of a particular elemental EDS peak, so each pixel in an image is either ‘on’ or off’ for carbon. The 3D reconstructions are built primarily from morphological features visible in SEM, measured slice-by slice.

2.6. Confocal laser Raman microspectroscopy

Confocal laser Raman microspectroscopy was performed on a *WITec alpha 300RA+* instrument with a *Toptica Photonics Xtra II* 785 nm laser source at the CMCA, UWA. Laser excitation intensity at the sample surface was in the 1-5 mW range, well below the intensity that may damage carbonaceous material (e.g., Everall et al., 1991) and comparable to previous studies of the Apex chert (e.g., Olcott Marshall et al., 2012; Sforna et al., 2014). The laser was focused through a 100x/0.9 objective to obtain a spot size of smaller than 1 μm. Spectral acquisitions were obtained with 600 l/mm grating and a peltier-cooled (-60 °C) 1024 x 128 pixel CCD detector. Laser centering and spectral calibration were performed daily on a silicon chip with characteristic Si Raman band of 520.4 cm^{-1}. Count rates were optimised prior to point spectra acquisition or hyperspectral mapping using the dominant quartz Raman band of 465 cm^{-1}. Spectra were collected in the 100-1800 rel. cm^{-1} region in order that both 1st order mineral vibration modes and 1st order carbonaceous vibration modes could be examined simultaneously. Raman maps were acquired with the spectral centre of the detector adjusted to 944 cm^{-1}, with a motorised stage allowing XYZ displacement with precision of better than 1 μm. A total of 15 filaments were mapped in 2D with each map containing between 13,440 and 22,400 individual spectra. Spectral decomposition and subsequent image processing were performed using WITec Project FOUR software, with baseline subtraction using a 3rd or 4th order polynomial. Carbon maps were created by integrating over the ~1600 cm^{-1} 'G' Raman band. The ~1350 cm^{-1} carbon 'D' Raman band was not used to construct maps because this may suffer from interference from the ~1320 cm^{-1} hematite Raman band in these samples (cf. Marshall and Olcott Marshall, 2013). All analyses were conducted on material embedded below the surface of the thin section to avoid artefacts in the Raman spectra resulting from polishing and/or surface contamination.

For 3D analysis, successive scans of nine filaments were performed at increasing z-depth within the thin section, with a 1 μm z-spacing interval. Only filaments occurring entirely in the top ~15 μm of the thin sections were analysed, partly because of loss of Raman signal and spatial resolution at greater depth (Schopf et al., 2005; Marshall and Olcott Marshall, 2013), and partly so that FIB-SEM data (which is also far easier to obtain in the upper 15 μm of a thin section) could be subsequently collected from some of the same filaments. 3D Raman data were segmented and visualised in *AVIZO 8.0*.

3. Results

3.1. Petrography

Micro-mapping of petrographic thin sections through our new material (sample CHIN-3) reveal equivalent fabrics to those found in the previously described ‘microfossil’ type sections of the Apex chert (Brasier et al., 2005). Multiple generations of brecciation, fissure filling and chert veining are evident. The majority of each thin section comprises a fissure filling fabric (fabric A of Brasier et al., 2005) that includes dark brecciated microcrystalline silica clasts rich in carbon and heavy metals (Fig. 2, A1), plus subsequent paler generations of microcrystalline silica (Fig. 2, A2-3) that infilled early voids within the breccia. Multiple veins of clear microquartz (Fabric B of Brasier et al., 2005) are present, and clear microquartz also infills some larger cavities (Fig. 2, B). The filaments described here are found only in fabric A, with the vast majority occurring in generation A2 (Fig. 2).

Filamentous microstructures (referred to as filaments from here on) are common in sample CHIN-3 (Figs. 3-7). Filament diameters range from 1.4 μm to 13 μm, with a mean of 4.2 μm (n=140). Filament lengths range from 9 μm to 97.5 μm with a mean of 33 μm (n=140). A size frequency distribution of the population of CHIN-3 filaments shows close similarity to previous studies of the Apex 'microfossils' (Fig. 8; cf. Schopf, 1993; Brasier et al., 2006). CHIN-3 filaments are a variety of colours, from pale grey (e.g., Fig. 3n) to dark brown (e.g., Fig. 7i) to almost black (e.g., Fig. 6k). Iron staining is also common, resulting in large numbers of filaments having an orange/pale brown (e.g., Fig. 6l) or even yellow coloration (e.g., Fig. 7j). Rarely, filaments change in colour along their length, exhibiting patches that are particularly dark or black interspersed with yellow or orange patches (Fig. 7j). This variety of coloration is comparable to the 'microfossil' holotypes where yellow (Fig. 5c) and orange iron-stained (Fig. 7c) specimens have been illustrated alongside dark brown and grey/black examples (Brasier et al., 2005, 2011). Filament distribution is also comparable to the 'microfossil' holotypes, occurring as solitary objects with random orientations. It is notable that a high proportion of the filaments from CHIN-3 are iron-stained. This is consistent with the large quantity of pyrite in this sample indicating a plentiful supply of iron in this part of the hydrothermal system. The lighter colour of many of the CHIN-3 filaments compared to the 'microfossil' holotypes may be due to the fact that our images come from 30 μm-thick thin sections as opposed to the 193-380 μm-thick thin sections used in earlier studies (Schopf, 1993; Brasier et al., 2005, 2011).

Crucially, CHIN-3 filaments exhibit the same diagnostic morphological features as those shown by the 'microfossil' holotypes and paratypes and subsequently used by Schopf (1993) to erect the 11 taxa of the Apex chert 'microbiota'. These features include disc-shaped, quadrate and short cylindrical medial 'cells' (Figs. 3-7); attenuation of filaments towards their apices (Fig. 3a-g); a variety of terminal 'cell' shapes including rounded, pillow-shaped and conical (e.g., arrows in Figs. 4-5); and evidence for ‘bifurcating cells’ and ‘cell pairs’ (Fig. 6h-m). In Figures 3-7 we show multiple examples of filaments from CHIN-3 that are directly equivalent to the holotypes of 8 out of the 11 Apex chert ‘microfossil’ taxa. These include filaments equivalent to *Primaevifilum attenuatum* (Fig. 3a-g), *Primaevifilum delicatum* (Fig. 3h-n), *Primaevifilum laticellosum* (Fig. 4a-f), *Primaevifilum conicoterminatum* (Fig. 4g-m), *Primaevifilum amoenum* (Fig. 6a-g), *Archaeoscillatoriopsis grandis* (Fig. 5a-g) *Archaeoscillatoriopsis disciformis* (Fig. 5h-n), and *Archaeoscillatoriopsis maxima* (Fig. 7a-d). We also illustrate filaments from CHIN-3 that are equivalent in morphology to unnamed ‘microfossils’ reported from the Apex chert in Schopf and Packer (1987) (Fig. 7e-m), plus examples of ‘bifurcating cells’ equivalent to those illustrated in Schopf (1993) (Fig. 6h-m).

Of the remaining 3 taxa of Apex ‘microfossils’ that are not illustrated here, a biological origin for *Eoleptonema apex* has already been disproven. This object has been shown to be a carbon-filled crack (Steele et al., 2008) and hence does not have the same formation mechanism as the material illustrated in this study. We do not observe filaments with diagnostic features and very narrow 0.5-0.6 μm diameters equivalent to *Archiotrichion septatum.* Some of our narrowest filaments from CHIN-3 (<1.8 μm) likely equate to the *Primaevifilum minutum* taxa of Schopf (1993) but these lack the defining morphological features of the wider filaments so we have not focused our efforts on these.

The combined evidence shows that the new filaments described here from CHIN-3 are equivalent to the holotypes and paratypes of the Apex chert ‘microfossils’ of Schopf and Packer (1987) and Schopf (1993). This means that interpretations and conclusions drawn from subsequent high spatial resolution study of this new material can also be applied to the previously described type material. Specifically, use of CHIN-3 enables application of destructive techniques on purported microfossil specimens that are prohibited on the type material. This is in contrast to some recent studies of the Apex chert where new types of filamentous pseudofossils were described but these exhibited little morphological resemblance to the type ‘microfossil’ material (Pinti et al., 2009; Marshall et al., 2011).

3.2. Detailed filament morphology and chemistry

Previous studies of the Apex ‘microfossils’ have relied upon optical microscopy and laser Raman microspectroscopy to decode their morphology and chemistry (e.g., Brasier et al., 2002; Schopf et al., 2002, 2007; Schopf and Kudryavtsev, 2009, 2012), while SEM and TEM have not previously been applied to Apex material. Both SEM, and especially TEM, provide much higher spatial resolution data and here reveal morphological and chemical features that are essentially invisible when viewed using light microscopy or Raman.

TEM analyses of ultrathin wafers through four representative filaments from CHIN-3 reveal filament morphologies that are characteristic of a mineralic origin, plus complex nano-scale intergrowths of mineral phases (Figs. 9-10). Each filament is made up of multiple plate- or sheet-like grains of phyllosilicate (Figs. 9-10, green), sitting within a matrix of microcrystalline quartz. Sometimes, quartz is also seen inter-grown with the phyllosilicate within a filament (Fig. 10d). ChemiSTEM mapping shows that the phyllosilicate mineral contains the elements K, Al, Si, O, plus variable amounts of Ba and minor Mg (Fig. 9). Electron diffraction patterns of this mineral obtained in the TEM (Fig. 10f-g) possess d-spacings consistent with a 2:1 layered phyllosilicate crystal lattice structure. This structure is found both in micas and some clay minerals (Downs et al., 1993). The nano-morphology of the phyllosilicate, appearing as a worm-like stack of crystals, closely resembles vermiculite, a common alteration product of mica (Medeiros et al., 2009). However, the chemical composition is spatially heterogenous on the nano- to micro-scale. Together with the presence of barium that was likely hydrothermally sourced (Van Kranendonk, 2006; Griffith and Paytan, 2012), this suggests that the phyllosilicate is a complex hydrothermal association of mica alteration products that are best termed vermiculite-like.

Further ChemiSTEM mapping shows that carbon (Figs. 9-10, yellow) and iron oxides (Figs. 9-10, red) are closely associated with the phyllosilicate filaments. Both carbon and iron are seen interleaved between sheets of phyllosilicates within the body of the filaments, and also coat the outer margins of some parts of the filaments. In addition, carbon frequently occurs away from the filaments within the quartz matrix (Figs. 9b,f, 10b, 11a-b) where it forms a boundary phase between quartz grains. ChemiSTEM mapping also gives insights into the relative timing of the introduction of carbon into these filaments. Carbon is frequently found coating barium-rich phyllosilicate grains and coating iron oxide particles (Fig. 11c-e), indicating that at least some of the carbon was the latest of all of the phases to become associated with the filaments.

FIB-SEM data reveal further complexities to the filaments and additional insights into carbon distribution (Figs. 12-13). For these analyses, hundreds of successive 200 nm thick slices were milled through four representative filaments (filaments 8, 15, 33 and

97; shown petrographically in Figs. 6e, 4k, 3d and 6g respectively). After each slice was cut an SEM image was acquired. These images demonstrate how the morphology of the filaments changes quite significantly over spatial scales of only a few micrometres. In some slices, their filamentous nature is clear and the sheet-like phyllosilicate grains appear neatly stacked (Fig. 13b, slices 133 and 143). In other slices, filaments are seen to branch (Fig. 13a, slice 85, labelled 'branch'), abruptly thicken (Fig, 12a, slice 8, compare top and bottom of image) or be joined by additional microstructures (Fig. 12a, slice 137, centre right). Furthermore, SEM highlights a number of nano-cracks within the chert matrix (Fig. 12a, slice 88 and Fig. 13a, slice 85); these commonly feed right into the filaments and are frequently filled with carbon, once again highlighting the fact that carbon can be a rather late phase in the vicinity of the filaments. Like the TEM data, the SEM data show significant amounts of carbon interleaved between phyllosilicate sheets (e.g., black material in Fig. 13b, slices 133 and 143), around the margins of the filaments (e.g., Fig. 13a, slice 85), and dotted throughout the quartz matrix (e.g., Fig. 13b, slice 45).

Raman microspectroscopy was performed in order to compare the distribution and thermal maturity of carbon in our new CHIN-3 material to that in previous studies of the holotype 'microfossils' (e.g., Brasier et al., 2002; Schopf et al., 2002, 2007; Schopf and Kudryavtsev, 2009, 2012). Raman spectra obtained from the filaments across the 100-1800 cm^{-1} spectral region exhibit vibrational bands at ~1350 cm^{-1} (carbon 'D' or 'disordered' band) and ~1600 cm^{-1} (carbon 'G' or 'graphitic' band) characteristic of kerogenous carbonaceous materials (Fig. 14) and are comparable to previous Raman analyses of the Apex 'microfossils' (e.g., fig. 4 of Brasier et al., 2002; fig. 3 of Schopf et al., 2002; fig. 6 of Schopf and Kudryavtsev, 2009).

Quantitative comparisons are not possible because detailed parameters (e.g. exact D and G peak positions and widths, plus D/G intensity ratios) are not reported in those previous publications, and small changes in the position of the carbon D band can be caused by the use of different lasers (e.g., our 785 nm laser compared to the 488.1 nm, 514.5 nm or 531 nm lasers of previous studies; cf. Pocsik et al., 1998). Quantitative comparisons are also hindered by potential inaccuracies in carbon D band parameters induced by the presence of hematite (having a major vibrational band at ~1320 cm^{-1}, very close to the carbon D band) in some Apex samples (cf. Marshall and Olcott Marshall, 2013). Nevertheless, the Raman data show that our new filaments contain carbon of very similar thermal maturity to both that found in the Apex ‘microfossil’ holotypes (e.g., Schopf et al., 2002), and to indigenous carbon reported elsewhere in the Apex black chert veins (e.g., Olcott Marshall et al., 2012; Sforna et al., 2014).

Raman mapping using the c. 1600 cm^{-1} carbon G band confirms that carbon is correlated with filamentous morphology in CHIN-3 (Fig. 14a-j). In some filaments the Raman maps indicate moderate amounts of carbon rather homogenously distributed throughout the body of the filament (Fig. 14i-j). This is equivalent to most Raman maps of the ‘microfossil’ holotypes (e.g., fig 2 of Schopf et al., 2002) where the ‘microfossils’ appear to be rather solid carbonaceous filaments. In several other CHIN-3 filaments, the distribution of carbon is heterogenous with carbon-rich portions separated by carbon-poor portions (Fig. 14a-h). In these cases the maps most closely resemble those presented previously for the holotypes of *Primaevifilum amoenum* and *Primaevifilum conicoterminatum* (fig 4h-l, o-t of Schopf et al., 2007) where the box-like carbon-poor zones in the maps were interpreted as cellular compartments now filled with quartz. A three-dimensional reconstruction of sequential Raman maps through filament 8 (Fig. 15a-b) closely resembles that previously produced for *Primaevifilum amoenum* (fig. 4g of Schopf et al., 2007). Like *P. amoenum*, filament 8 appears to comprise a number of box-like mineral-filled compartments (Fig. 15b, arrows) separated by carbon. In the absence of other data, these compartments may be mistaken for cell lumina. However, it is particularly notable that the distribution of carbon in the Raman maps does not resemble the distribution of carbon in the higher spatial resolution SEM and TEM images (compare for example Fig. 14 with Fig. 9, and Fig. 15b with 15c-g). This important point will be discussed further below (Section 4.2). Finally, Raman mapping also shows that there is a significant amount of carbon distributed outside of the filaments within the quartz matrix. Raman spectra from this carbon are almost identical to those from carbon found within and along the edge of the filaments (Fig. 14k), consistent with previous observations (Brasier et al., 2002).

Reconstruction and three-dimensional visualisation of the FIB-SEM data highlights some features of the CHIN-3 filaments that are not visible in standard optical images or Raman maps. For example, filament 8 is seen to have a short branch close to its uppermost termination that is only visible from certain viewpoints in x,y,z space (Fig. 15d,f, white arrow). This branch runs from the main long axis of the filament almost vertically down into the thin section. Hence, it is hidden from view when the filament is viewed in optical microscopy or visualised looking down the z-axis from above (compare Figs 15c and d). These 3-dimensional visualisations make it clear that this structure is a branch and cannot be attributed to folding of the filament (cf. Schopf quoted in Dalton, 2002). This filament also has an offset close to its lowermost termination that is seen in optical images and confirmed by the 3D model (Figs. 15a and c, red arrow). Again, it is very apparent that the distribution of carbon as shown by these 3D FIB-SEM visualisations is very different to that seen in the lower spatial resolution 3D Raman visualisation (compare Fig. 15b with 15c-g). Filament 15 has a significant branch that runs from close to its medial point almost vertically down into the thin section (Fig. 16a-d). There are hints of this branch in the optical image and in the 3D model viewed down the z-axis (Fig. 16a-b, arrows) but the branch becomes much clearer, and an origin due to folding of the filament can be dismissed, when the 3D model is rotated (Fig. 16c-d, branch circled). Likewise, filament 33 has a short branch extending from close to its medial point at a high angle down into the thin section (Fig. 16e-h). Again, there are hints of this branch in the optical image (Fig. 16e, arrow) but it is much more evident in the 3D model (Fig. 16f-g, arrow). In all three of these filaments the sheet like nature of carbon distribution is also highlighted in the 3D visualisations (Fig. 15g, 16d,h arrows).

4. **Discussion**

4.1. Cellular nature of the Apex filaments?

Schopf and Kudryavtsev (2012) state that resolution of the Apex microfossil controversy hinges on ‘whether the Apex fossils are cellular and composed of kerogenous carbon’. In a follow up comment Schopf and Kudryavtsev (2013) state there is an ‘extensive body of data establishing the biogenicity of the demonstrably cellular carbonaceous Apex fossils’. These statements about cellularity are now discussed in light of our new data.

Our new SEM and TEM data disprove the claim that the Apex filaments are cellular. Despite significant carbon being associated with the filaments, the distribution of this carbon is incompatible with cellular filamentous prokaryotes.

When examined at the nano-scale, carbon associated with *bona fide* microfossils is restricted to particular domains that correspond to cell or sheath walls and is largely absent from the interior of the cells/sheaths (Oehler et al., 2006; Wacey et al., 2012). In well-preserved permineralised (i.e. three dimensionally preserved) primitive prokaryote specimens the carbon forms rounded continuous microstructures (see for example fig. 12 of Wacey et al., 2012) while in more poorly preserved specimens these microstructures may be interrupted by mineral growth, yet still retain an overall cylindrical or ovoid shape in cross section (see figs 13-14 of Wacey et al., 2012). Carbon is rarely redistributed far from the microfossil walls. In marked contrast, the carbon associated with the Apex filaments is equally abundant in the interior of the filaments as along the filament margins. There are no rounded continuous carbonaceous microstructures, with most carbon taking on a rather linear, sheet-like or spikey appearance. Furthermore, multiple sheet-like carbonaceous features traversing the width of the filament are not organised in a manner consistent with cross walls of a chain of cells. Not only are there far too many carbonaceous sheets to match the number of cell walls viable in filaments of this length, the gaps between the sheets are very variable, with some of the sheets <50 nm apart. For a *bona fide* chain of cells, the cross walls of adjacent cells would likely be at least an order of magnitude further apart.

The relative age of carbon with respect to the other mineral phases is also incompatible with fossilised microbial cells. The silicate mineral grains making up the majority of the filament appear to have been formed before much of the iron oxide and carbon and this is incompatible with patterns of precipitation of silicates within cells (cf. Wacey et al., 2014). Furthermore, the morphology and composition of the silicates are consistent with a hydrothermal formation mechanism and less consistent with biologically induced precipitation. It is possible that some primary carbonaceous material fell into the hydrothermal vents along with phyllosilicates and other minerals from the country rocks. However, the presence of carbon of identical thermal maturity outside of the filaments, along quartz grain boundaries, indicates that carbon distribution was heavily influenced by mineral crystallisation and any primary carbonaceous material has been significantly redistributed within the hydrothermal system. The presence of carbon along nano-fractures leading into some filaments shows that mobile carbon was present in the system for a considerable period of time after the initial formation of the filaments. This indicates, along with data from some recent studies (e.g., Sforna et al., 2014), that carbon now associated with Apex filaments is unlikely to have been fossilised *in situ* as previously claimed (Schopf and Kudryavtsev, 2012).

4.2. How accurate is laser Raman mapping of ancient putative microfossils?

As noted in Section 3.2, laser Raman mapping reveals significantly different distributions of carbon within the filaments to those obtained through TEM or SEM analysis. Both SEM and TEM analyses show that carbon mostly occurs as distinct narrow linear bands and sheets interspersed with phyllosilicates and occasional quartz (e.g., Figs 9-10, 12-13, 15g, 16d,h). In contrast, both 2D and 3D Raman maps of the same filaments (Figs. 14, 15b) blur these linear carbon features into more homogenous carbon-rich zones, and alternating carbon-rich and carbon-poor zones are only resolved at the micrometer scale rather than the nanometer scale. In addition, Raman mapping does not accurately replicate the morphology of the filaments in three dimensions, frequently failing to resolve parts of the filaments, especially key features such as branches buried deeper within the thin section under the main axis of a filament (e.g., compare Fig. 15b with 15d).

These differences can, in part, be attributed to the differences in spatial resolution capabilities of the three techniques. Both SEM and TEM are capable of resolving nm-scale features. In this study, pixels in the SEM images mostly corresponded to around 20 nm of material, while those in the TEM images were commonly less than 5 nm. This means that narrow carbonaceous features and other very small mineral grains could easily be resolved. Similarly, ChemiSTEM elemental mapping in the TEM can detect coatings of carbon ~5 nm thick, enabling the relative timings of e.g., Ba, Fe and C to be decoded. In contrast, the lateral spatial resolution of our laser Raman instrument is only about 500 nm and the vertical resolution around 1 μm, while that of previous Raman analyses is even coarser (e.g., Schopf et al., 2002, quoted lateral resolution <1 μm, and vertical resolution 1-3 μm). This in turn leads to less accurate maps and an amalgamation of tiny linear features into larger rounded zones. Furthermore, due to the effects of spherical aberration, Raman suffers from a decrease in spatial resolution and a drop in signal intensity with depth (Schopf et al., 2005), so that the accuracy of Raman maps deteriorates further with increasing depth within a thin section. It has been shown that, under typical Raman analysis conditions, data collected at a depth in excess of 15 μm below the surface of a thin section will be unusable for constructing Raman maps (Marshall and Olcott Marshall, 2013). Further, for the carbon G band, the depth at which accurate maps can be constructed may be limited to about 6 μm below the surface (Marshall and Olcott Marshall, 2013). These limitations of Raman explain why features lying below the main axis of the filaments in CHIN-3 are not resolved in Raman maps, and why some filaments that plunge into the thin section cannot be mapped for carbon along their entire length.

It has been claimed that there are ~1900 'cells' in 174 microfossil specimens in studied samples of the Apex chert (Schopf and Kudryavtsev, 2013), yet Raman maps from only 6 specimens have ever been published (Schopf et al., 2002, 2007; Schopf and Kudryavtsev, 2009, 2012). Of these, two show specimens apparently made of solid carbon with no cellularity (figs 2g and 2i of Schopf et al., 2002), while another two show specimens mostly comprising carbon with occasional small angular gaps, interpreted to be filled with quartz, but incompatible with the morphology of cell lumina (figs 3h and 3k of Schopf and Kudryavtsev, 2012). Only two specimens contain features in Raman maps that resemble cell lumina (figs 4g-i and 4o-t of Schopf et al., 2007) and even here it is noticeable how thick the supposed 'cell walls' are compared to the inferred quartz-filled lumina, and how blocky or box-like the inferred lumina are compared to the equivalent light microscope images. It is also notable that the box-like 'cell lumina' are of a similar size to the quoted lateral spatial resolution of the Raman instrument and are, in some cases, smaller than the quoted vertical resolution of the instrument. Hence, a 'cell lumina' in a Raman map only equates to a handful of pixels or voxels in the image. In addition, the accuracy of the 3D model of *Primaevifilum amoenum* (fig. 4g of Schopf et al., 2007) may be questioned because the focal spacing between successive images was 0.75 μm but the quoted vertical spatial resolution of the instrument was 1-3 μm. Even without this caveat, the published 3D model of *Primaevifilum amoenum* does not demonstrate its cylindrical nature as claimed (Schopf et al., 2007) because it is never shown in multiple orientations and the cross sectional morphology of the filament is never illustrated.

In many of the previous Raman maps of the Apex ‘microfossils’ one can observe carbon outside of the analysed filament. This is evident in both 2D maps (e.g., white material around the edges of figs 2f and 2i of Schopf et al., 2002) and sequential images of 3D datasets (e.g., pale grey material in fig. 4h-l of Schopf et al., 2007). Furthermore, some of the carbon at the margins of the filaments has a rather spikey morphology, appearing to extend from the filament in narrow linear bands into the surrounding quartz matrix (e.g., fig. 4s of Schopf et al., 2007).

It was also claimed that Raman spectra could distinguish kerogenous carbonaceous materials having a biological precursor from those with abiotic formation mechanisms (Schopf et al., 2002). This claim has since been disproved by laser Raman specialists (e.g., Pasteris and Wopenka, 2003) and it has been shown that Raman cannot distinguish disordered biological material from other poorly ordered carbons produced by processes such as redox reactions during serpentinization (Pasteris, 1998), inorganic deposition from high temperature fluids (Wopenka and Pasteris, 1993), geological deposition from hydrothermal solutions (Brasier et al., 2002) or high temperature heating of precursor compounds (Beny-Bassez and Rouzaud, 1985). Of course, the Raman spectra of Apex carbon are *consistent* with a biological precursor origin. Hence, it is possible that some or all of the carbon within the Apex 'microfossil' type samples may ultimately have a biological origin, but it has been redistributed to such an extent that no primary biological morphologies have been preserved. This places the Apex chert carbon in a similar category to that of the c. 3.82 Ga Akilia supracrustal rocks (Mojzis et al., 1996; Manning et al., 2006) in terms of providing only ambiguous geochemical evidence for life on the early Earth.

Our current work, together with that of others cited above, shows that neither Raman point spectra nor Raman mapping is capable of determining the biogenicity of a putative carbonaceous microfossil. More crucially, this current work shows that misinterpretations of the structure of putative microfossils may occur when Raman and optical data are obtained in isolation from higher spatial resolution data. In the case presented here, selected CHIN-3 filaments could plausibly be interpreted to contain box-like 'cell lumina' when only Raman maps are considered (e.g., Fig. 14c-j; Fig. 15b). However, this hypothesis is disproven when SEM and/or TEM data from the same filaments is taken into account, and a mineralic origin for the filaments becomes clear. Previous reports of the 'microfossil' holotypes likely also suffer from these Raman-induced misinterpretations (e.g., Schopf et al., 2002, 2007; Schopf and Kudryavtsev, 2009, 2012).

4.3. A new formation mechanism for the Apex 'microfossils'

The data presented here requires us to reject a microfossil origin for the Apex filaments. Rather, the data points towards a multi-stage hydrothermally-controlled mechanism. We propose that this begins with hydrothermal production of K- and Ba-rich micas of the Warrawoona Group. These are known to include interstitial, micron-sized potassium- and barium-rich micas precipitated in siliceous layers of the Marble

Bar Chert (Orberger et al., 2004, 2006; Van Kranendonk, 2006); and potassium micas found in hydrothermally altered and highly silicified Warrawoona Group basalts, both as pseudomorphs after plagioclase laths, needles and aggregates, and as micron-scale blades and fibers inter-grown with quartz grains in veinlets (Nakamura and Kato, 2004; see their fig. 3f). Following transportation, these hydrothermally-produced micas were subjected to further hydrothermal alteration, in turn becoming hydrated phyllosilicates termed vermiculites (e.g. Prakash Narashima et al., 2006). These common hydrothermal alteration products have a similar crystal structure to the precursor micas but have additional hydrated cations (usually Mg) in the crystal lattice (De la Calle and Suquet, 1988). It is also notable that a very similar mineral (termed hydro-muscovite by the authors) has been reported as a common alteration product of both biotite and K-feldspar in the Kitty's Gap chert of the nearby 3.45 Ga Panorama Formation (Oberger et al., 2006). The additional hydrated cations of minerals such as vermiculite give them the remarkable ability to exfoliate (i.e. undergo accordion-like expansion at right angles to their cleavage plane) when heated rapidly, as this additional water is converted to steam (Prakash Narashima et al., 2006). Once exfoliated, the morphology of vermiculite strongly resembles a worm (hence, vermiculite from the Latin vermiculare 'to breed worms'), which in turn matches the morphology of the filaments in the Apex chert.

In the Apex hydrothermal system, pulses of hydrothermal activity would first alter the mica to vermiculite and subsequently heat the vermiculite causing exfoliation. Once exfoliated, vermiculite has a very high surface area and a high adsorption capacity resulting from the strong capillary action of slit-like pores between plate-like grains (Medeiros et al., 2009). Today vermiculite is used for a number of industrial purposes, but of particular relevance here is its use for cleaning up oil spills (e.g., Zhao et al., 2011). Likewise, in the Apex hydrothermal system, these microscopic worm-like vermiculite grains would have a strong affinity for any carbon that was moving around the system, and carbon would be adsorbed and held on the mineral surface. This is consistent with the distribution of carbon that we see in our TEM and SEM maps where it appears as linear or sheet-like features with a strong locational affinity for the slit like pores between adjacent phyllosilicate crystals.

5. Conclusions

We have here demonstrated that filamentous microstructures, previously thought to be Earth's oldest microfossils, are in fact mineral artefacts comprising stacks of phyllosilicate grains with carbonaceous coatings.

We have analysed new material from the Apex chert 'microfossil locality' that contains filaments identical to the holotypes and paratypes of at least 8 out of the 11 taxa of the 'Apex chert microbiota' erected by Schopf (1993). By applying state-of-the-art electron microscopy techniques (not permitted on the type specimens) to this new material we have revealed the 3D nano-structure and chemistry of the filaments. All filaments analysed are made up of multiple plate-like grains of a vermiculite-like phyllosilicate, with occasional intergrowths of quartz, enclosed within a quartz matrix. Several of the microstructures are not simple filaments as originally claimed, but are branched in ways that are incompatible with a primitive bacterial origin.

Carbon occurs within the filaments as narrow (~10's nm) bands and sheets in between the phyllosilicate grains with a distribution incompatible with known filamentous prokaryote morphology. It also occurs as irregular coatings at the boundaries of the filaments, at junctions between quartz grains within the matrix, and in late stage nano-fractures. The carbon Raman signature is comparable to previous studies, indicating that the carbon may ultimately have had a biological origin, but these data are equally consistent with the carbon forming during abiogenic hydrothermal synthesis. Whatever the primary origin of the carbon, the combined data indicate that it is either a late phase and/or has been redistributed to such an extent that no original biological morphology could be preserved. Rather than being fossilised prokaryote organisms, we interpret the filaments as resulting from the alteration and exfoliation of flakes of mica, plus the redistribution of barium, iron and carbon during repeated episodes of fluid movement within a hydrothermal system.

This work has important implications for the evaluation of primitive life on Earth and, by extension, in extra-terrestrial settings. Herein, candidate microfossils that appear to pass most currently accepted biogenicity criteria when examined at the micrometer scale, have been shown to fail several criteria when examined at the sub-micrometer scale. Hence, future work should focus on the refinement of biogenicity criteria using *bone-fide* microfossils and definitive non-biological microfossil-like artefacts examined at the sub-micrometer scale. In this context we caution against the use of laser Raman mapping as stand alone chemical evidence to support the biogenicity of ancient putative microfossils. This technique lacks the spatial resolution to accurately map the distribution of carbon in such samples and should, at the very least, be supported by higher spatial resolution analytical techniques.

Acknowledgements

We acknowledge the facilities, scientific and technical assistance of the Australian Microscopy & Microanalysis Research Facility at: Centre for Microscopy Characterisation and Analysis, The University of Western Australia; Electron Microscopy Unit, The University of New South Wales. These facilities are funded by the Universities, State and Commonwealth Governments. DW was funded by the European Commission and the Australian Research Council (FT140100321). This is ARC CCFS paper number XXX. We acknowledge Martin van Kranendonk, Owen Green, Cris Stoakes, Nicola McLoughlin, the late John Lindsay and the Geological Survey of Western Australia for fieldwork assistance, Thomas Becker for assistance with Raman microspectroscopy, Anthony Burgess from *FEI* for the preparation of one of the TEM wafers, and Russell Garwood, Tom Davies, Imran Rahman & Stephan Lautenschlager for training and advice on the *SPIERS* and *AVIZO* software suites. We thank Chris Fedo and an anonymous reviewer for comments that improved the manuscript.

References

Barghoorn, E.S., Tyler, S.A., 1965. Microorganisms from the Gunflint Chert. Science 147, 563–577.

Beny-Bassez, C., Rouzaud, J.N., 1985. Characterization of carbonaceous materials by correlated electron and optical microscopy and Raman microspectroscopy. Scanning Electron Microscopy 1985, 119–132.

Berndt, M.E., Allen, D.E., Seyfried, W.E., 1996. Reduction of CO_2 during serpentinization of olivine at 300°C and 500 bar. Geology 24, 351–354.

Brasier, M.D., Green, O.R., Jephcoat, A.P., Kleppe, A.K., Van Kranendonk. M.J., Lindsay, J.F., Steele, A., Grassineau, N.V., 2002. Questioning the evidence for Earth's oldest fossils. Nature 416, 76–81.

Brasier, M.D., Green, O.R., McLoughlin, N., 2004. Characterisation and critical testing of potential microfossils from the early Earth: the Apex ‘microfossil debate’ and its lessons for Mars sample return. International Journal of Astrobiology 3, 1–12.

Brasier, M.D., Green, O.R., Lindsay, J.F., McLoughlin, N., Steele, A., Stoakes, C., 2005. Critical testing of earth's oldest putative fossil assemblage from the similar to 3.5 Ga Apex Chert, Chinaman Creek, western Australia. Precambrian Research 140, 55–102.

Brasier, M.D., McLoughlin, N., Green, O., Wacey, D., 2006. A fresh look at the fossil evidence for early Archaean cellular life. Philosophical Transactions of the Royal Society B 361, 887–902.

Brasier, M.D., Green, O.R., Lindsay, J.F., McLoughlin, N., Stoakes, C., Brasier, A., Wacey, D., 2011. Geology and putative microfossil assemblage of the c. 3460 Ma ‘Apex chert’, Chinaman Creek, Western Australia - a field and petrographic guide. Geological Survey of Western Australia, Record 2011/7, 60p.

Brasier, M.D., Matthewman, R., McMahon, S., Kilburn, M., Wacey, D., 2013. Pumice from the ~3460Ma Apex Basalt, Western Australia: a natural laboratory for the early biosphere. Precambrian Research 224, 1–10.

Brasier, M.D., Antcliffe, J., Saunders, M., Wacey, D., 2015. Changing the picture of Earth's earliest fossils (3.5–1.9 Ga) with new approaches and new discoveries. Proceedings of the National Academy of Sciences USA 112, 4859–4864.

Brydson, R., 2001. Electron Energy Loss Spectroscopy. Springer, New York, 160pp.

Dalton, R., 2002. Squaring up over ancient life. Nature 417, 782–784.

De Gregorio, B.T., Sharp, T.G., 2006. The structure and distribution of carbon in the 3.5 Ga Apex chert: Implications for the biogenicity of Earth's oldest putative microfossils. American Mineralogist 91, 784–789.

De Gregorio, B.T., Sharp, T.G., Flynn, G.J., Wirick, S., Hervig, R.L., 2009. Biogenic origin for Earth's oldest putative microfossils. Geology 37, 631–634.

De la Calle, C., Suquet, H., 1988. Vermiculites. In: Bailey, S.W (Ed.), Reviews in Mineralogy: Hydrous Phyllosilicates, vol. 19. Mineralogical Society of America, Washington, p. 725. Chap 12.

de Vries, S.J., 2004. Early Archaean sedimentary basins: depositional environment and hydrothermal systems – examples from the Barberton and Coppin Gap greenstone belts. Utrecht University, Geologica Ultraiectina 244, 160p.

Downs, R.T., Bartelmehs, K.L., Gibbs, G.V., Boisen, M.B., 1993. Interactive software for calculating and displaying X-ray or neutron powder diffractometer patterns of crystalline materials. American Mineralogist 78, 1104–1107.

Everall, N.J., Lumsdon, J., Christopher, D.J., 1991. The effect of laser-induced heating upon the vibrational raman spectra of graphites and carbon fibres. Carbon 29, 133–137.

Griffith, E.M., Paytan, A., 2012. Barite in the ocean – occurrence, geochemistry and palaeoceanographic applications. Sedimentology 59, 1817–1835.

Jannasch, H.W., Wirsen, C.O., 1981. Morphological survey of microbial mats near deep-sea thermal vents. Applied Environmental Microbiology 41, 528–538.

Knoll, A.H., Strother, P., Rossi, S., 1988. Distribution and diagenesis of fossils from the lower Proterozoic Duck Creek Dolomite, Western Australia. Precambrian Research 38, 257–259.

Manning, C.E., Mojzis, S.J., Harrison, T.M., 2006. Geology, age and origin of supracrustal rocks at Akilia, West Greenland. American Journal of Science 306, 303–336.

Marshall, C.P., Olcott Marshall, A., 2013. Raman hyperspectral imaging of microfossils: potential pitfalls. Astrobiology 13, 920–931.

Marshall, C.P., Emry, J.R., Olcott Marshall, A., 2011. Haematite pseudomicrofossils present in the 3.5-billion-year-old Apex Chert. Nature Geoscience 4, 240–243.

Medeiros, M.D., Sansiviero, M.T.C., Araujo, M.H., Lago, R.M., 2009. Modification of vermiculite by polymerisation and carbonization of glycerol to produce highly efficient materials for oil removal. Applied Clay Science 45, 213–219.

Mojzis, S.J., Arrhenius, G., McKeegan, K.D., Harrison, T.M., Nutman, A.P., Friend, C.R.L., 1996. Evidence for life on Earth before 3,800 million years ago. Nature 384, 55–59.

Nakamura, K., Kato, Y., 2004. Carbonatization of oceanic crust by the seafloor hydrothermal activity and its significance as a CO_2 sink in the Early Archean. Geochimica et Cosmochimica Acta 68, 4595–4618.

Oberger, B., Pinti, D.L., Gallien, J.-P., Wagner, C., Fialin, M., Daudin, L., Hashizume, K., 2004. Micropaleoenvironments of an Archaean chert: a key for understanding δ^{15}N signatures. Workshop on the Origin of Life, Foundation Treilles, 2-7 March, France.

Orberger, B., Rouchon, V., Westall, F., de Vries, S.T., Pinti, D., Wagner, C., Wirth, R., Hashizume, K., 2006. Microfacies and origin of some Archean cherts (Pilbara, Australia). In: Processes on the Early Earth: Geol. Soc. Am. Spec. Paper 405 (eds. Reimold, W.U., Gibson, R.L.), p.133–156.

Oehler, D.Z., Robert, F., Mostefaoui, S., Meibom, A., Selo, M., McKay, D.S., 2006. Chemical mapping of Proterozoic organic matter at sub-micron spatial resolution. Astrobiology 6, 838–850.

Olcott Marshall, A., Emry, J.E., Marshall, C.P., 2012. Multiple generations of carbon in the Apex chert and implications for preservation of microfossils. Astrobiology 12, 160–166.

Olcott Marshall, A., Marshall, C.P., 2013. Comment on “Biogenicity of Earth’s earliest fossils: a resolution of the controversy” by J William Schopf and Anatoliy B Kudryavtsev, Gond. Res. 22, 761-771. Gondwana Research 23, 1654–1655.

Olcott Marshall, A., Jehlicka, J., Rouzaud, J-N., Marshall, C.P., 2014. Multiple generations of carbonaceous material deposited in Apex chert by basin-scale pervasive hydrothermal fluid flow. Gondwana Research 25, 284–289.

Pasteris, J.D., 1998. The laser Raman microprobe as a tool for the economic geologist. In: Applications of Microanalytical Techniques to Understanding Mineralizing Processes, edited by M.A. McKibben, W.C. Shanks, and W.I. Ridley, Society of Economic Geologists, Littleton, CO, pp.233–250.

Pasteris, J.D., Wopenka, B., 2002. Images of the earth’s oldest fossils? (discussion and reply). Nature 420, 476–477.

Pasteris, J.D., Wopenka, B., 2003. Necessary, but not sufficient: Raman identification of disordred carbon as a signature of ancient life. Astrobiology 3, 727–738.

Pinti, D.L., Mineau, R., Clement, V., 2009. Hydrothermal alteration and microfossil artefacts of the 3,465-million-year-old Apex chert. Nature Geoscience 2, 640–643.

Pinti, D.L., Mineau, R., Clement, V., 2013. Comment on “Biogenicity of Earth’s earliest fossils: a resolution of the controversy” by J. William Schopf and Anatoliy B Kudryavtsev, Gond. Res. 22, 761-771 (2012). Gondwana Research 23, 1652–1653.

Pocsik, I., Hundhausen, M., Koos, M., Ley, L., 1998. Origin of the D peak in the Raman spectrum of microcrystalline graphite. Journal of Non Crystalline Solids 227–230, 1083–1086.

Prakash Narashima, K.N., Ramalingaiah, H., Melka, K., Krishnaveni, K., Prasad, P.S.R., Krishnaiah, C., Jayappa, K.S., Ganesha, A.V., 2006. Vermiculite mineralization associated with ultramafics in Agasthyapura area, Mysore Dist., Karnataka State, India – A mineralogical study. Acta Geodynamica et Geomaterialia 3, 19–31.

Schopf, J.W., Packer, B.M., 1987. Early Archean (3.3-billion to 3.5-billion-year-old) microfossils from Warrawoona Group, Australia. Science 237, 70–73.

Schopf, J.W., 1992. Paleobiology of the Archaean. In: The Proterozoic Biosphere: a multidisciplinary study (ed. JW Schopf and C Klein), pp25-39. Cambridge University Press, New York.

Schopf, J.W., 1993. Microfossils of the Early Archean Apex Chert – new evidence of the antiquity of life. Science 260, 640–646.

Schopf, J.W., 1999. The Cradle of Life. Princeton University Press, New York, 367p.

Schopf, J.W., 2006. Fossil evidence of Archaean life. Philosophical Transactions of the Royal Society B 361, 869–885.

Schopf, J.W., Kudryavtsev, A.B., 2009. Confocal laser scanning microscopy and Raman imagery of ancient microscopic fossils. Precambrian Research 173, 39-49.

Schopf, J.W., Kudryavtsev, A.B., 2012. Biogenicity of Earth's earliest fossils: A resolution of the controversy. Gondwana Research 22, 761–771.

Schopf, J.W., Kudryavtsev, A.B., 2013. Reply to the comments of D.L. Pinti, R. Mineau and V. Clement, and of A.O. Marshall and C.P. Marshall on ”Biogenicity of Earth’s earliest fossils: a resolution of the controversy” by J.William Schopf and Anatoliy B. Kudryavtsev, Gond. Res. 22 (2012), 761-771. Gondwana Research 23, 1656–1658.

Schopf, J.W., Kudryavtsev, A.B., Agresti, D.G., Wdowiak, T.J., Czaja, A.D., 2002. Laser-Raman imagery of Earth's earliest fossils. Nature 416, 73–76.

Schopf, J.W., Kudryavtsev, A.B., Agresti, D.G., Czaja, A.D., Wdowiak, T.J., 2005. Raman imagery: a new approach to assess the geochemical maturity and biogenicity of permineralized Precambrian fossils. Astrobiology 5, 333–371.

Schopf, J.W., Kudryavtsev, A.B., Czaja, A.D., Tripathi, A.B., 2007. Evidence of Archaean life: stromatolites and microfossils. Precambrian Research 158, 141–155.

Sforna, M.C., van Zuilen, M.A., Philippot, P., 2014. Structural characterization by Raman hyperspectral mapping of organic carbon in the 3.46 billion-year-old Apex chert, Western Australia. Geochimica et Cosmochimica Acta 124, 18–33.

Steele, A., Fries, M., Schweizer, M., Green, O., Lindsay, J., Wacey, D., Brasier, M., 2008. The limits of microRaman imaging of ancient or not so fossils / pseudofossils. Results from a study of the Apex and Strelley cherts. Astrobiology 8, 324.

Sutton, M.D., Garwood, R.J., Siveter, D.J., Siveter, D.J., 2012. SPIERS and VAXML: A software toolkit for tomographic visualization and a format for virtual specimen interchange. Palaeontologica Electronica 15(2):5T.

Thorpe, R.I., Hickman, A.H., Davis, D.W., Mortensen, J.K., Trendall, A.F., 1992. U-Pb zircon geochronology of Archaean felsic units in the Marble Bar region, Pilbara Craton, Western Australia. Precambrian Research 56, 169–189.

Van Kranendonk, M.J., 2006. Volcanic degassing, hydrothermal circulation and the flourishing of early life on Earth: A review of the evidence from c. 3490-3240 Ma rocks of the Pilbara Supergroup, Pilbara Craton, Western Australia. Earth Science Reviews 74, 197–240.

Van Kranendonk, M.J., Smithies, R.H., Hickman, A.H., Champion, D.C., 2007. Review: secular tectonic evolution of Archean continental crust: interplay between horizontal and vertical processes in the formation of the Pilbara Craton, Australia. Terra Nova 19, 1–38.

Wacey, D., 2009. Early life on Earth: A practical guide. Springer, 285p.

Wacey, D., Kilburn, M.R., Saunders, M., Cliff, J., Brasier, M.D., 2011. Microfossils of sulfur metabolizing cells in ~3.4 billion year old rocks of Western Australia. Nature Geoscience 4, 698–702.

Wacey, D., Menon, S., Green, L., Gerstmann, D., Kong, C., McLoughlin, N., Saunders, M., Brasier, M.D., 2012. Taphonomy of very ancient microfossils from the ~3400 Ma Strelley Pool Formation and ~1900 Ma Gunflint Formation: new insights using focused ion beam. Precambrian Research 220–221, 234–250.

Wacey, D., Saunders, M., Roberts, M., Menon, S., Green, L., Kong, C., Culwick, T., Strother, P., Brasier, M.D., 2014. Enhanced cellular preservation by clay minerals in 1 billion-year-old lakes. Nature Scientific Reports 4, 5841.

Wopenka, B., Pasteris, J.D., 1993. Structural characterization of kerogens to granulite-facies graphite: applicability of Raman microprobe spectroscopy. American Mineralogist 78, 533–557.

Zhao, M-Q., Huang, J-Q., Zhang, Q., Luo, W-L., Wei, F., 2011. Improvement of oil adsorption performance by a sponge-like natural vermiculite-carbon nanotube hybrid. Applied Clay Science 53, 1–7.

Figure Legends

Fig. 1. Geological context for the Apex chert 'microfossils'. (a) Overview of the East Pilbara Terrane of the Pilbara Craton, Western Australia showing the location of the Apex chert at Chinaman Creek (arrow) (modified from Van Kranendonk et al., 2007 and Wacey, 2009). (b) Stratigraphy of the Marble Bar greenstone belt, Pilbara, Western Australia. The Apex chert (unofficial name) is found in the lower portion of the Apex Basalt. (Age dates come from Thorpe et al., 1992; de Vries, 2004; plus a collection of Geological Survey of Western Australia zircon geochronological results summarised in Van Kranendonk et al., 2007) (c) Geological map of the north block of the Apex Basalt around Chinaman Creek in the Marble Bar greenstone belt. The 'microfossil' locality is found in a black chert vein (N1) at some 50–100 m palaeodepth below the stratiform Apex chert. (d) Photograph looking approximately south of the north block of the Apex Basalt. Chinaman Creek is in the foreground with the N1 black chert vein outlined in red and the stratiform chert in pale yellow.

The ‘microfossil’ locality is marked with a star. (c-d) Modified from Brasier et al., 2005.

Fig. 2. Petrographic context for filaments in sample CHIN-3. The thin section is dominated by fissure fill fabrics (Fabric A of Brasier et al., 2005) including dark brecciated microcrystalline silica clasts rich in carbon and heavy metals (A1), plus subsequent paler generations of microcrystalline silica (A2-3) that infilled early voids within the breccia. Veins of clear microquartz (Fabric B of Brasier et al., 2005) are present elsewhere in the thin section, while clear microquartz also infills some larger cavities (B). Filaments directly equivalent to the ‘microfossil’ holotypes and paratypes of Schopf (1993) occur in early A fabrics, mostly A2. Examples of filaments analysed in detail in this study are numbered. Larger objects that may be part of the same morphological spectrum as the filaments are arrowed.

Fig. 3. Apex chert ‘microfossil’ holotypes (Schopf, 1993) and equivalent filaments from our new material (part 1 of 5). (a-b) *Primaevifilum attenuatum* holotype and accompanying interpretative sketch (Schopf, 1993). (c) *Primaevifilum attenuatum* holotype reimaged using *Automontage* software (Brasier et al., 2002) showing potential side-branch omitted from the image in (a) plus iron staining. (d-g) Filaments equivalent to *Primaevifilum attenuatum* from sample CHIN-3. Note the attenuation of filaments towards their apices, a feature that was erected as a defining characteristic of this species (Schopf, 1993, Table 1). Star indicates filament investigated using high spatial resolution electron microscopy in this study. (h-i) *Primaevifilum delicatulum* holotype and accompanying interpretative sketch (Schopf, 1993). (j) *Primaevifilum delicatulum* holotype reimaged using *Automontage* software (Brasier et al., 2002)

showing additional adjoining microstructures omitted in (h). Dashed box indicates area shown in (h). (k-n) Filaments equivalent to *Primaevifilum delicatulum* from sample CHIN-3. Small red numbers simply refer to the naming convention of the filaments.

Fig. 4. Apex chert ‘microfossil’ holotypes (Schopf, 1993) and equivalent filaments from our new material (part 2 of 5). (a-b) *Primaevifilum laticellulosum* holotype and accompanying interpretative sketch (Schopf, 1993). (c) *Primaevifilum laticellulosum* holotype reimaged using *Automontage* software (Brasier et al., 2002). (d-f) Filaments equivalent to *Primaevifilum laticellulosum* from sample CHIN-3. Note pillow-shaped terminal ‘cells’ (arrows), a feature that was erected as a defining characteristic of this species (Schopf, 1993, Table 1). (g-h) *Primaevifilum conicoterminatum* holotype and accompanying interpretative sketch (Schopf, 1993). (i) *Primaevifilum conicoterminatum* holotype reimaged using Automontage software (Brasier et al., 2002). (j-m) Filaments equivalent to *Primaevifilum conicoterminatum* from sample CHIN-3. Note conical terminal ‘cells’ (arrows), a feature that was erected as a defining characteristic of this species (Schopf, 1993, Table 1). Star indicates filament investigated using high spatial resolution electron microscopy in this study. Small red numbers simply refer to the naming convention of the filaments.

Fig. 5. Apex chert ‘microfossil’ holotypes and paratypes (Schopf, 1993) plus equivalent filaments from our new material (part 3 of 5). (a-b) *Archaeoscillatoriopsis grandis* paratype and accompanying interpretative sketch (Schopf, 1993). (c) *Archaeoscillatoriopsis grandis* paratype reimaged using *Automontage* software showing microstructure to have a pale yellow colour (Brasier et al., 2011). (d-g)

Filaments equivalent to *Archaeoscillatoriopsis grandis* from sample CHIN-3. Star indicates that filament 96 was investigated using electron microscopy in this study, and the yellow line indicates the position of the extracted TEM wafer shown in Figure 10c-g. (h-i) *Archaeoscillatoriopsis disciformis* holotype and accompanying interpretative sketch (Schopf, 1993). (j) *Archaeoscillatoriopsis disciformis* holotype reimaged using *Automontage* software (Brasier et al., 2002) showing that this filament has a side branch, possible lower extension, and appears to outline a rhombic crystal ghost (red arrow). Dashed box shows area imaged in (h). (k-n) Filaments equivalent to *Archaeoscillatoriopsis disciformis* from sample CHIN-3. Note the hemispheroidal to globular terminal ‘cells’ (black arrows), a feature that was erected as a defining characteristic of this species (Schopf, 1993, Table 1). Small red numbers simply refer to the naming convention of the filaments.

Fig. 6. Apex chert ‘microfossil’ holotypes (Schopf, 1993) plus equivalent filaments from our new material (part 4 of 5). (a-b) *Primaevifilum amoenum* holotype and accompanying interpretative sketch (Schopf, 1993). (c) *Primaevifilum amoenum* holotype reimaged using *Automontage* software (Brasier et al., 2002) showing possible side branch (arrow). (d-g) Filaments equivalent to *Primaevifilum amoenum* from sample CHIN-3. Stars indicate filaments investigated using high spatial resolution electron microscopy in this study. (h-i) Examples of bifurcated cells and cell pairs (arrows) as stated in Schopf (1993) and reimaged using *Automontage* software (Brasier et al., 2011). (j-m) Examples of ‘bifurcated cells’ and ‘cell pairs’ (arrows) from filamentous microstructures within sample CHIN-3. (n) Filament 155, with yellow line indicating position of the extracted TEM wafer shown in Figure 10a-b. (o) Filament 101, with yellow line indicating position of the extracted TEM wafer

shown in Figure 9. Small red numbers simply refer to the naming convention of the filaments.

Fig. 7. Apex chert 'microfossil' holotype (Schopf, 1993) and unnamed paratypes (Schopf and Packer, 1987) plus equivalent filaments from our new material (part 5 of 5). (a-b) *Archaeoscillatoriopsis maxima* holotype and accompanying interpretative sketch (Schopf, 1993). (c) *Archaeoscillatoriopsis maxima* holotype reimaged using *Automontage* software showing significant iron staining (Brasier et al., 2011). (d) Filament equivalent to *Archaeoscillatoriopsis maxima* from sample CHIN-3. (e) Unnamed microfossil from Schopf and Packer (1987). (f-g) Filaments equivalent to the object shown in (e) from sample CHIN-3. (h) Unnamed microfossil from Schopf and Packer (1987), (i-j) Filaments equivalent to the object shown in (h) from sample CHIN-3. (k) Unnamed microfossil from Schopf and Packer (1987). (l-m) Filaments equivalent to the object shown in (k) from sample CHIN-3. Star indicates filament investigated using high spatial resolution electron microscopy in this study. Small red numbers simply refer to the naming convention of the filaments. (n-o) Microstructures in CHIN-3 with a partial filamentous nature but morphology incompatible with an interpretation as microfossils. In the central portion of (n) large phyllosilicate mineral grains (arrow) have disrupted the filamentous shape, while in (o) the microstructure is somewhat larger than previously reported for any of the type microfossils.

Fig. 8. Size frequency distribution of filaments from CHIN-3 (blue) compared to previous data from the Apex chert (red and green). Widths of modern prokaryote filaments and *bona fide* filamentous microfossils from the 1878 Ma Gunflint chert are also given for comparison (from Brasier et al., 2015).

Fig. 9. Chemistry of the filaments (part 1 of 2). (a) Dark-field scanning TEM image of an ultrathin (c. 100 nm) slice through filament 101 (see Fig. 6o for corresponding optical image). Note that in dark-field scanning TEM images low mass material is dark in colour and high mass material bright white. Hence, carbon will appear dark grey to black in such images. (b) False colour ChemiSTEM elemental overlay map of the area indicated in (a), where green is aluminium representing phyllosilicate, red is iron representing iron oxide, and yellow is carbon. The filament is seen to comprise book-like stacks of sheet-like phyllosilicate grains sitting in a quartz matrix (black). Carbon and iron are frequently found in between the sheets of phyllosilicate, as well as around parts of the margins of the filament and in the quartz matrix. (c-h) Individual false colour ChemiSTEM elemental maps of the filament showing that the phyllosilicate is potassium-rich and, in places, barium-rich.

Fig. 10. Chemistry of the filaments (part 2 of 2). (a) Dark-field scanning TEM image of an ultrathin (c. 100 nm) slice through filament 155 (see Fig. 6n for corresponding optical image). (b) ChemiSTEM elemental map of the area indicated in (a), where green is aluminium representing phyllosilicate, red is iron representing iron oxide, and yellow is carbon. Note how carbon and iron are frequently found as planar features in between sheets of phyllosilicates, as well as around the margins of the filament and in the matrix (arrow). (c) Dark-field scanning TEM image of an ultrathin (c. 100 nm) slice through part of filament 96 (see Fig. 5g for corresponding optical image). (d) ChemiSTEM elemental map of the area indicated by green box in (c) where green is aluminium from phyllosilicate, red is iron from iron oxide, and yellow is carbon. Here, a number of quartz grains (q) are intermixed with the phyllosilicate sheets

within the filament. Again, carbon and iron are found in between phyllosilicate sheets and around the margins of the filament. (e) Close up ChemiSTEM carbon map of the region of filament 96 indicated by the yellow box in (c), emphasizing the way narrow strings or sheets of carbon (yellow) are interleaved with phyllosilicate and quartz grains (black). (f-g) Selected area electron diffraction patterns from the regions of the TEM wafer indicated in (c). DP1 is consistent with the [001] zone axis pattern from a 2:1 phyllosilicate. DP2 shows a pattern of ring arcs, representative of a set of closely aligned grains of a 2:1 phyllosilicate with the beam incident parallel to the $\{00l\}$ plane (modified from Brasier et al., 2015).

Fig. 11. Carbon distribution and timing in the vicinity of the filaments. (a) Dark field scanning TEM image of the quartz matrix in the vicinity of filament 9 (the very edge of the filament can be seen in the bottom centre of the TEM image; see Fig. 14a for optical image of filament 9). Several micro-quartz grain boundaries are visible (dark curvi-linear features). (b) ChemiSTEM elemental map of the same area as (a) showing that carbon occurs at many of the quartz grain boundaries; iron is not associated within this carbon. In contrast, both iron and carbon occur at the margins of the aluminium-rich (green) phyllosilicate filament. (c-e) False colour three element overlays of parts of the filaments shown by the dashed boxes in Figs 9-10. In some zones, carbon (yellow) coats iron (red) in between sheets of phyllosilicates (green), while in others carbon (yellow) coats barium-rich phyllosilicate (blue) once again suggesting that carbon was the later phase.

Fig. 12. Three dimensional morphology of filament 8 (equivalent to *Primaevifilum amoenum* holotype) and filament 15 (equivalent to *Primaevifilum conicoterminatum*

holotype) from sample CHIN-3. (a) Backscatter SEM images of 3 out of 155 successive focused ion beam (FIB)-milled slices through filament 8. The space between slices is 200 nm so the 155 slices cover 31 μm of material parallel to the main trend of the filamentous microstructure. The approximate location of each of the figured slices (S8, S88 and S137) is shown on the optical image. (b) Backscatter SEM images of 3 out of 135 successive FIB-milled slices through filament 15. The slice spacing is 200 nm so the 135 slices cover 27 μm of material parallel to the main trend of the filamentous microstructure. The approximate location of each of the figured slices (S68, S83 and S109) is shown on the optical image. In both cases the data demonstrate the significant morphological variability at the nano-scale as one moves through the length of the filaments. In all slices, uniform mid-grey is the quartz matrix, slightly paler grey sheet-like material stacked together in complex book-like patterns is the phyllosilicates, black is carbon, and brightest grey/white is Fe- and Ba-rich heavy minerals. Carbon is clearly seen to coat many of the individual phyllosilicate sheets in the book-like stacks. Carbon also occurs at several grain boundaries in the quartz matrix and in a number of nano-cracks that, in places, join the filaments.

Fig. 13. Three dimensional morphology of filament 33 (equivalent to *Primaevifilum attenuatum* holotype) and filament 97 (equivalent to *Primaevifilum amoenum* holotype) from sample CHIN-3. a) Backscatter SEM images of 3 out of 200 successive FIB-milled slices through filament 33. The space between slices is 200 nm so the 200 slices cover 40 μm of material parallel to the main trend of the filamentous microstructure. The approximate location of each of the figured slices (S33, S85 and S123) is shown on the optical image. (b) Backscatter SEM images of 3 out of 168

successive FIB-milled slices through filament 97. The slice spacing is 200 nm so the 168 slices cover 33.6 μm of material parallel to the main trend of the filamentous microstructure. The approximate location of each of the figured slices (S45, S133 and S143) is shown on the optical image. As in Fig. 12, uniform mid-grey is the quartz matrix, slightly paler grey sheet-like material stacked together in complex book-like patterns is the phyllosilicates, black is carbon, and brightest grey/white is Fe- and Ba-rich heavy minerals. Carbon is clearly seen to coat many of the individual phyllosilicate sheets in the book-like stacks. Carbon also occurs at several grain boundaries in the quartz matrix and in a number of nano-cracks that, in places, join the filaments. Filament 33 is seen to branch at depth below the surface of the thin section (see slice 85, ‘branch’).

Fig. 14. Raman images and spectra from CHIN-3 filaments. (a) Transmitted light photomicrograph of filament 9. (b) Raman G band intensity map of the area marked by the blue box in (a), analyzed 6 μm below the surface of the thin section. (c) Transmitted light photomicrograph of filament 97. (d) Raman G band intensity map of the area marked by the blue box in (c), analyzed 3 μm below the surface of the thin section. (e) Transmitted light photomicrograph of filament 38. (f) Raman G band intensity map of the area marked by the blue box in (e), analyzed 6 μm below the surface of the thin section. (g) Transmitted light photomicrograph of filament 3. (h) Raman G band intensity map of the area marked by the blue box in (g), analyzed 4 μm below the surface of the thin section. (i) Transmitted light photomicrograph of filament 4. (j) Raman G band intensity map of the area marked by the blue box in (i), analyzed 3 μm below the surface of the thin section. Arrows in b, d, f and h indicate box-like carbon-poor zone of the filaments. Note that only sub-portions of a given

filament can be mapped at a single focal depth. (k) Typical Raman spectra in the 1st order carbon region from CHIN-3 filaments and matrix. The spectra are broadly comparable to one another and to previous Raman analyses of the Apex ‘microfossils’ (Brasier et al., 2002; Schopf et al., 2002). Variations in the D band shape may be due to interference from the 1320 cm^{-1} hematite band in the vicinity of the filaments (cf. Marshall and Olcott Marshall, 2013).

Fig. 15. Three-dimensional reconstruction of filament 8. (a) Transmitted light photomicrograph of filament 8. (b) 3D visualization of Raman images from filament 8 showing carbonaceous composition (red) and box-like mineral-filled compartments (arrows). (c) 3D visualization of FIB-SEM images from filament 8 shown in the same orientation as (a-b). Red arrow shows offset in filament, also seen in the optical image. (d-f) 3D FIB-SEM model rotated to show additional complexities to the filament not seen in (a-b). Of particular note is the small branch extending down below the main body of the filament (arrows in d,f). (g) Higher magnification visualization showing the sheet-like nature of much of the carbon in the filament (arrows).

Fig. 16. Three-dimensional reconstruction of filaments 15 and 33. (a) Transmitted light photomicrograph of filament 15. (b) 3D visualization of FIB-SEM images from filament 15 shown in the same orientation as (a). Note that a small side feature can be seen in both images (arrows). (c-d) 3D FIB-SEM model rotated to show the additional thick branch extending down below the main body of the filament (dashed circles). Note also the linear sheet-like nature of much of the carbon (arrow in d). (e) Transmitted light photomicrograph of filament 33. (f) 3D visualization of FIB-SEM

images from filament 33 shown in the same orientation as (e). Note that a small side feature is hinted at in the light micrograph (arrow) and is seen more clearly in the 3D model (arrow). (g) 3D FIB-SEM model rotated to more clearly demonstrate the short thick branch extending down below the main body of the filament (arrow). (h) Higher magnification visualization showing the sheet-like nature of much of the carbon, especially at the narrow end of the filament (arrow).

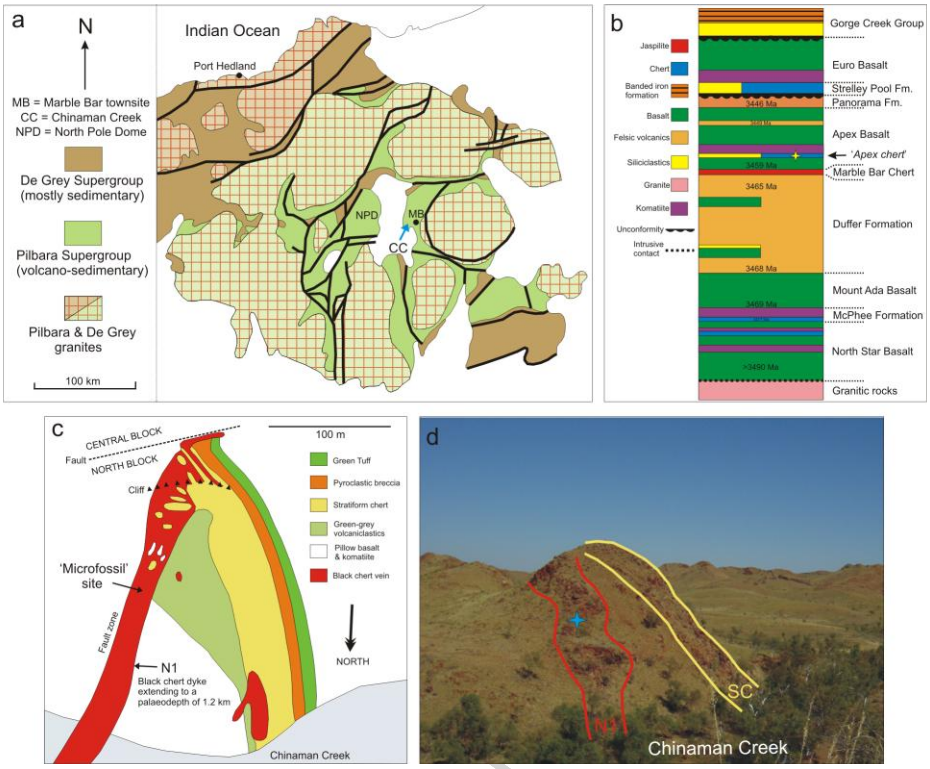
a
N
MB = Marble Bar townsite
CC = Chinaman Creek
NPD = North Pole Dome
De Grey Supergroup (mostly sedimentary)
Pilbara Supergroup (volcano-sedimentary)
Pilbara & De Grey granites
100 km
Indian Ocean
Port Hedland
NPD
MB
CC
b
Jaspilite
Chert
Banded iron formation
Basalt
Felsic volcanics
Siliciclastics
Granite
Komatiite
Unconformity
Intrusive contact
Gorge Creek Group
Euro Basalt
Strelley Pool Fm.
Panorama Fm.
3446 Ma
Apex Basalt
'Apex chert'
3459 Ma
Marble Bar Chert
3465 Ma
Duffer Formation
3468 Ma
Mount Ada Basalt
3469 Ma
McPhee Formation
North Star Basalt
>3490 Ma
Granitic rocks
c
CENTRAL BLOCK
Fault
NORTH BLOCK
Cliff
100 m
Green Tuff
Pyroclastic breccia
Stratiform chert
Green-grey volcaniclastics
Pillow basalt & komatiite
Black chert vein
'Microfossil' site
Fault zone
N1
Black chert dyke extending to a palaeodepth of 1.2 km
NORTH
Chinaman Creek
d
N1
SC
Chinaman Creek

Figure 1

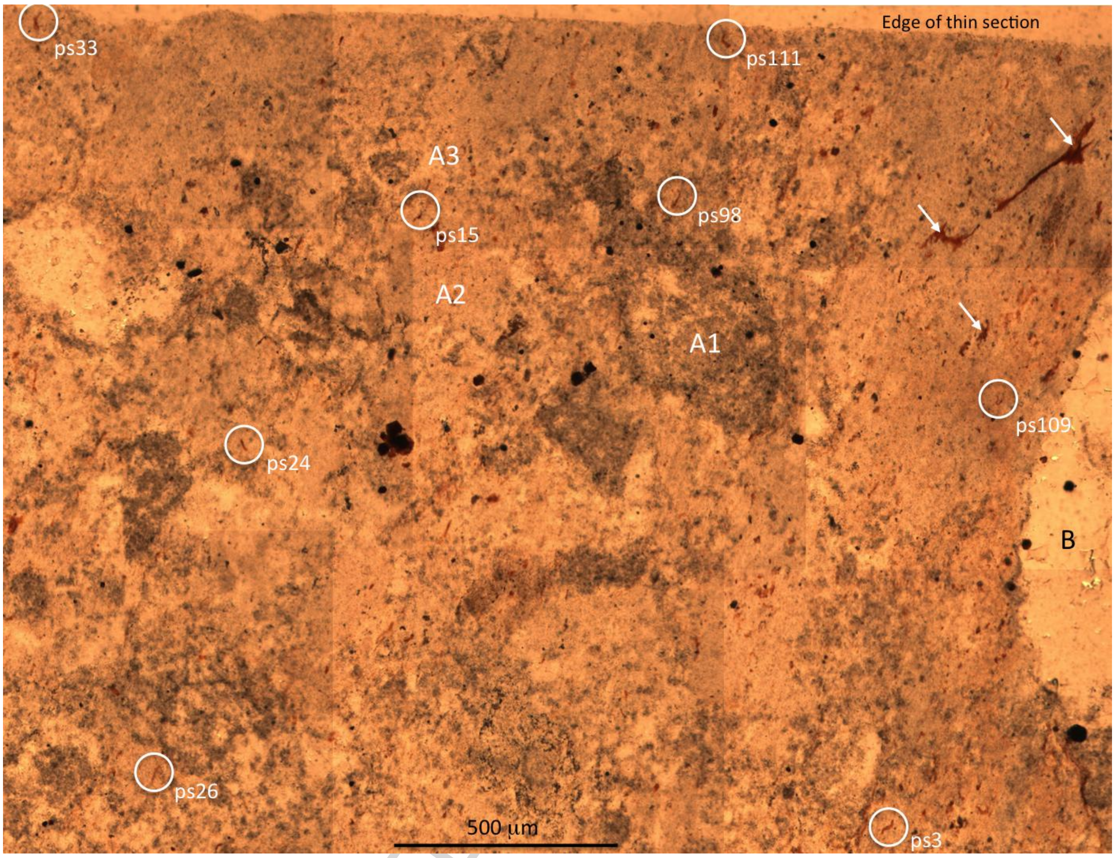
Edge of thin section
ps33
ps111
A3
ps15
ps98
A2
A1
ps109
ps24
B
ps26
500 µm
ps3

Figure 2

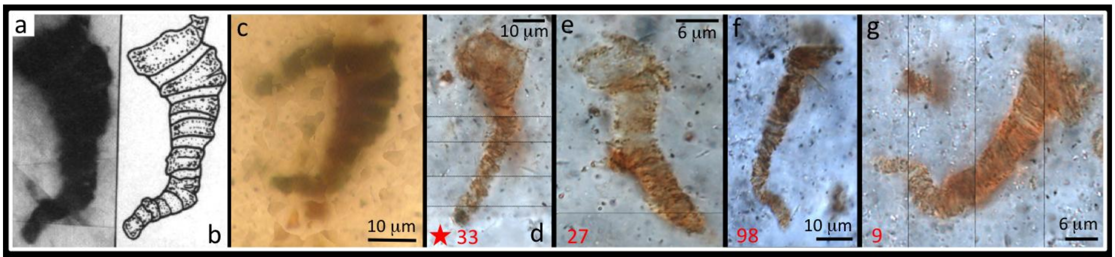

Primaevifilum attenuatum Distinguishing features (from Schopf, 1993): Marked attenuation of 'trichome'; Medial 'cells' 4-12 µm wide and disc shaped; Terminal 'cell' shape is flat rounded.

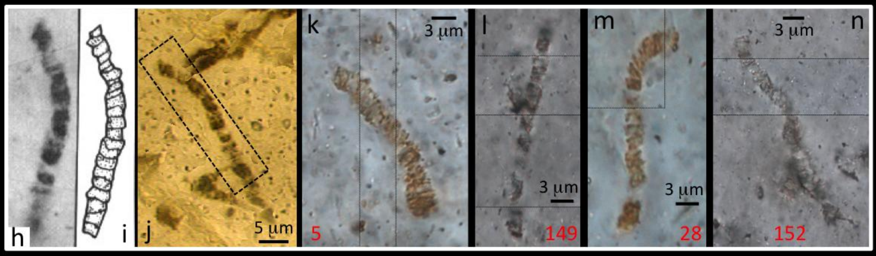

Primaevifilum delicatum Distinguishing features (from Schopf, 1993): Medial 'cells' 1.8-3.2 µm wide, disc shaped or short cylinder; Terminal 'cell' shape is flat or flat rounded; Filaments not tapered

Figure 3

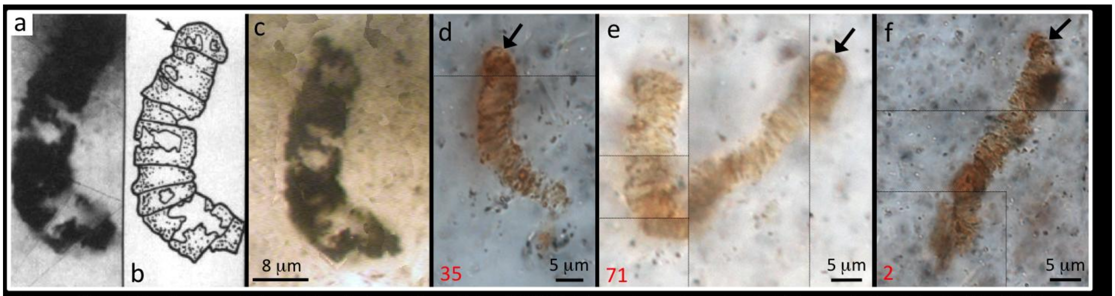

Primaevifilum laticellosum Distinguishing features (from Schopf, 1993): Pillow shaped terminal ‘cell’ (arrows); Medial cell width 6-8.5 µm, short cylinder or quadrate shaped; Filaments can be slightly attenuated towards apices

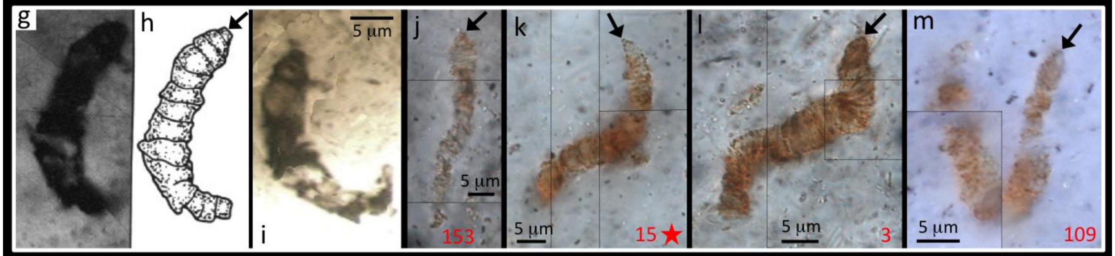

Primaevifilum conicoterminatum Distinguishing features (from Schopf, 1993): Medial ‘cells’ 4-6 µm wide, disc shaped or short cylinder; Terminal ‘cells’ conical or blunt rounded (arrows); Filaments can be attenuated towards apices

Figure 4

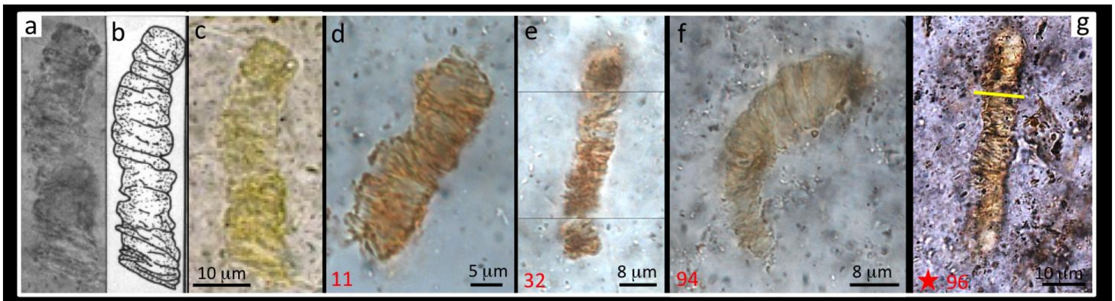

Archaeoscillatoriopsis grandis Distinguishing features (from Schopf, 1993): Medial 'cells' 8-11.5 µm wide and disc shaped; Terminal 'cell' shape flat rounded or hemispheroidal; Filaments not tapered towards apices

Archaeoscillatoriopsis disciformis Distinguishing features (from Schopf, 1993): Medial 'cells' 3-5.5 µm wide and disc shaped; Terminal 'cells' hemispheroidal or globular (see arrows); Filaments can be tapered towards apices

Figure 5

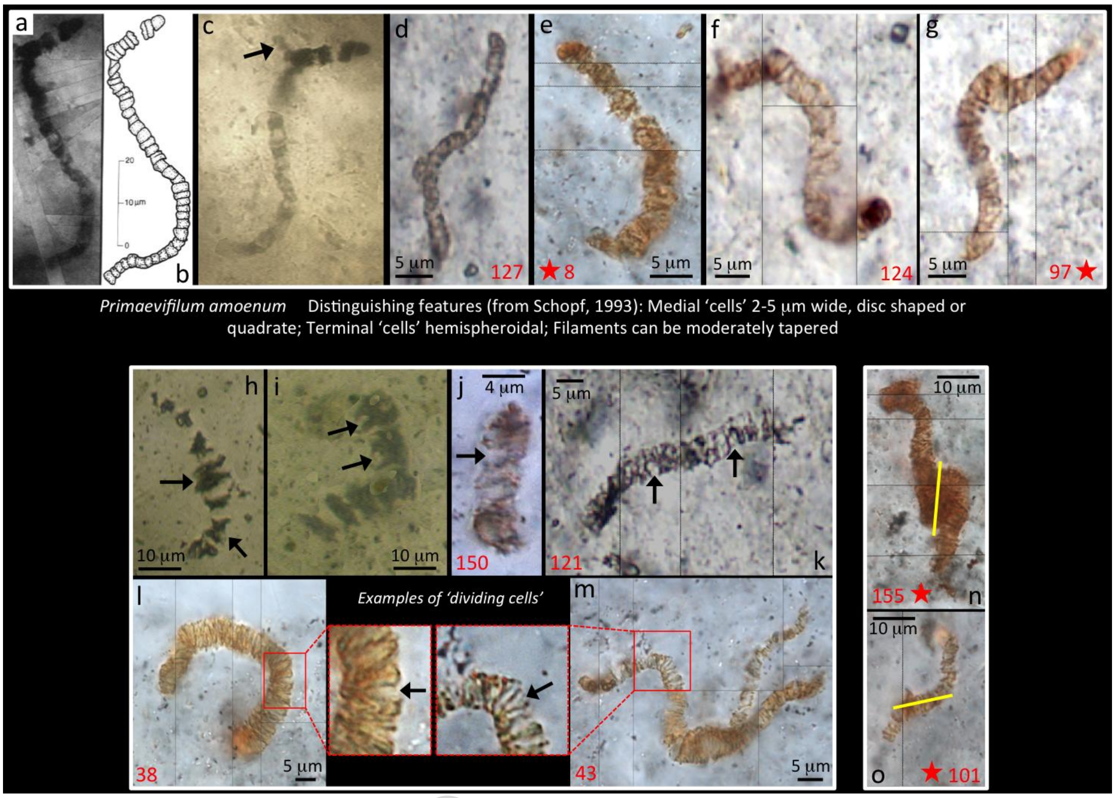

Primaevifilum amoenum Distinguishing features (from Schopf, 1993): Medial 'cells' 2-5 µm wide, disc shaped or quadrate; Terminal 'cells' hemispheroidal; Filaments can be moderately tapered

Examples of 'dividing cells'

Figure 6

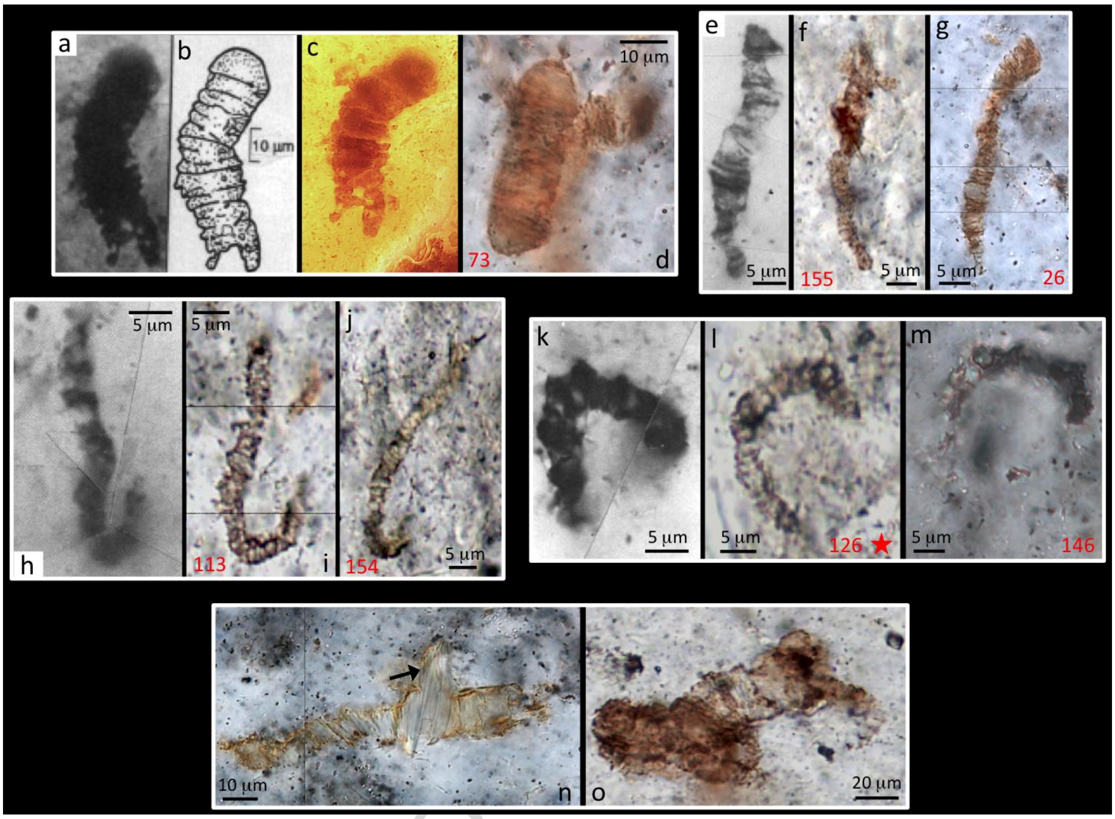
a
b
10 µm
c
10 µm
73
d
e
5 µm
f
155
5 µm
g
5 µm
26
5 µm
h
5 µm
113
i
j
154
5 µm
k
5 µm
l
5 µm
126 ★
m
5 µm
146
10 µm
n
o
20 µm

Figure 7

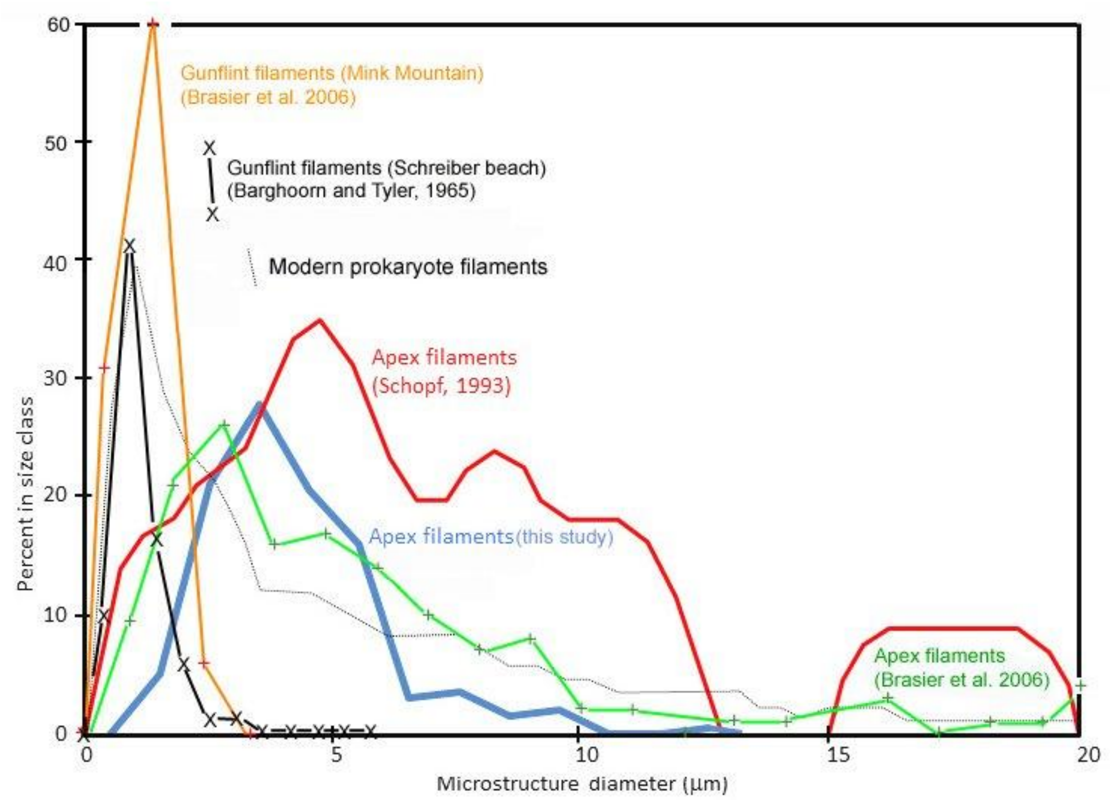
60
50
40
30
20
10
0
Percent in size class
0
5
10
15
20
Microstructure diameter (µm)
Gunflint filaments (Mink Mountain)
(Brasier et al. 2006)
Gunflint filaments (Schreiber beach)
(Barghoorn and Tyler, 1965)
Modern prokaryote filaments
Apex filaments
(Schopf, 1993)
Apex filaments(this study)
Apex filaments
(Brasier et al. 2006)

Figure 8

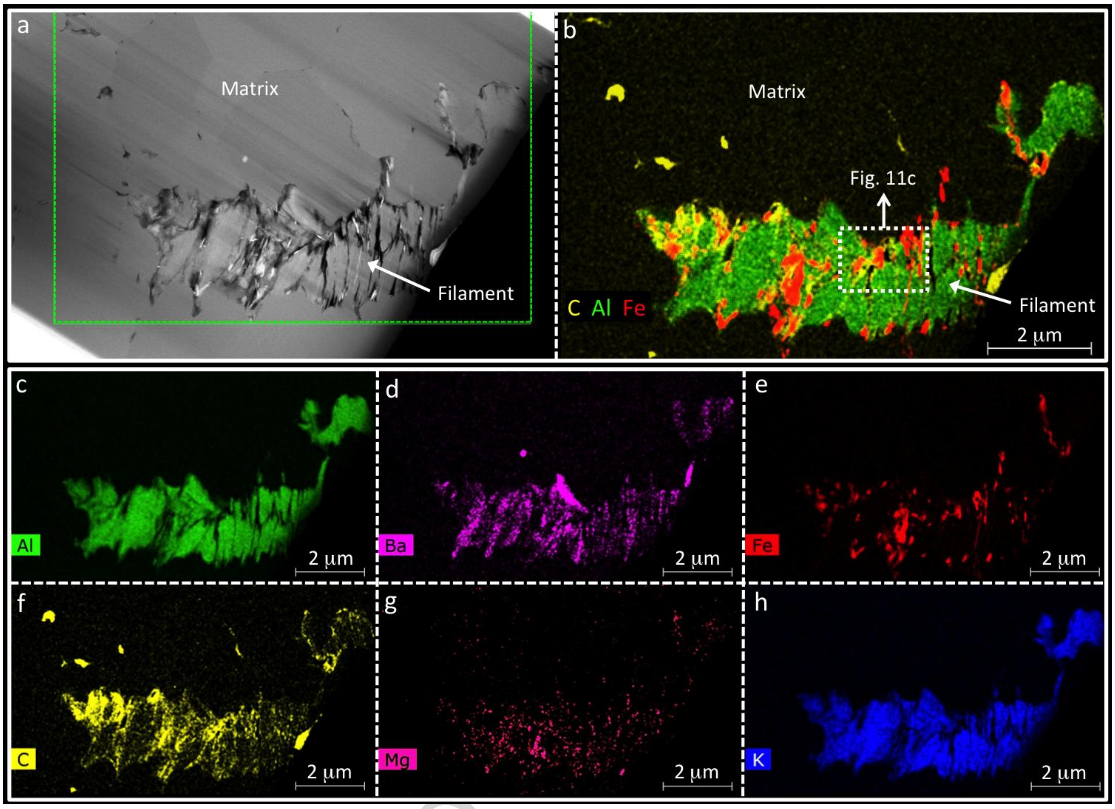
a
Matrix
Filament
b
Matrix
Fig. 11c
Filament
C Al Fe
2 µm
c
Al
2 µm
d
Ba
2 µm
e
Fe
2 µm
f
C
2 µm
g
Mg
2 µm
h
K
2 µm

Figure 9

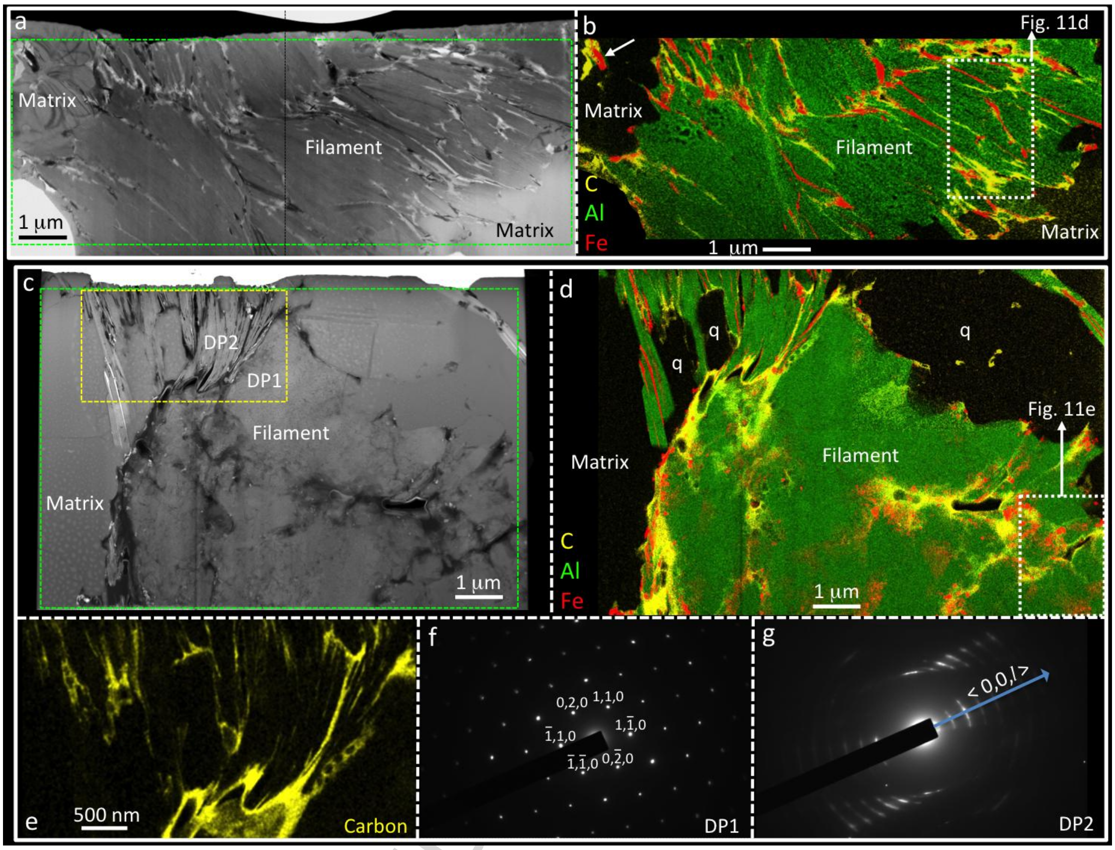
a
Matrix
Filament
1 µm
Matrix
b
Fig. 11d
Matrix
Filament
C
Al
Fe
1 µm
Matrix
c
DP2
DP1
Filament
Matrix
1 µm
d
q
q
q
Fig. 11e
Matrix
Filament
C
Al
Fe
1 µm
e
500 nm
Carbon
f
0,2,0
1,1,0
1̄,1,0
1,1̄,0
1̄,1̄,0
0,2̄,0
DP1
g
< 0,0,l >
DP2

Figure 10

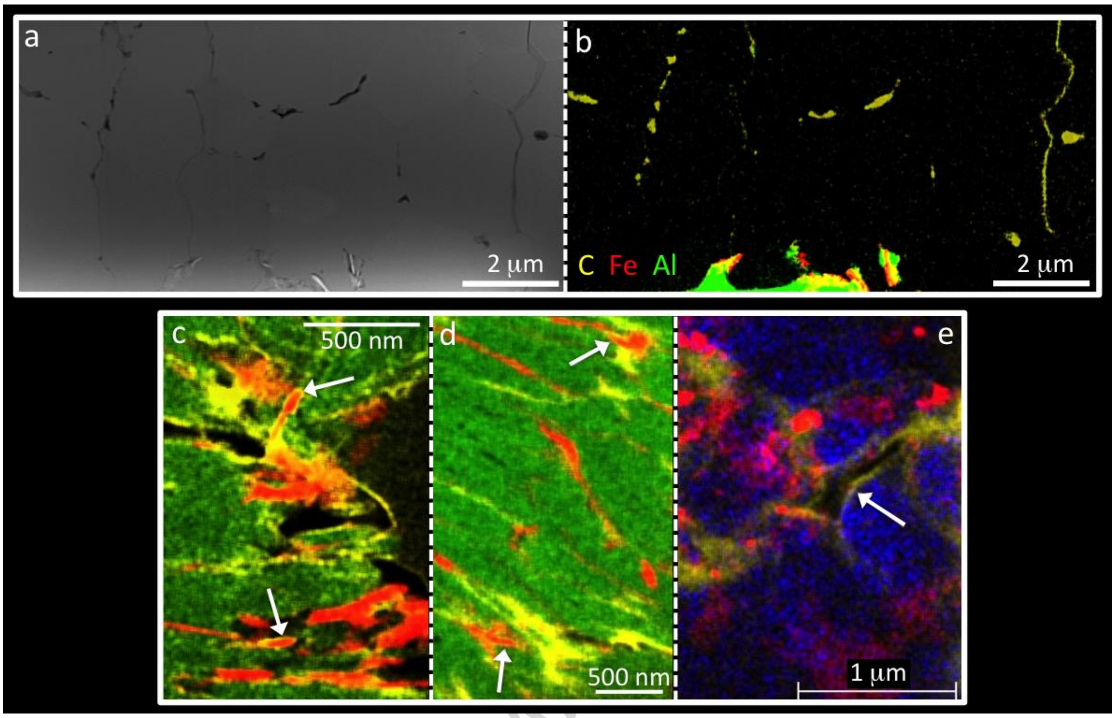

Figure 11

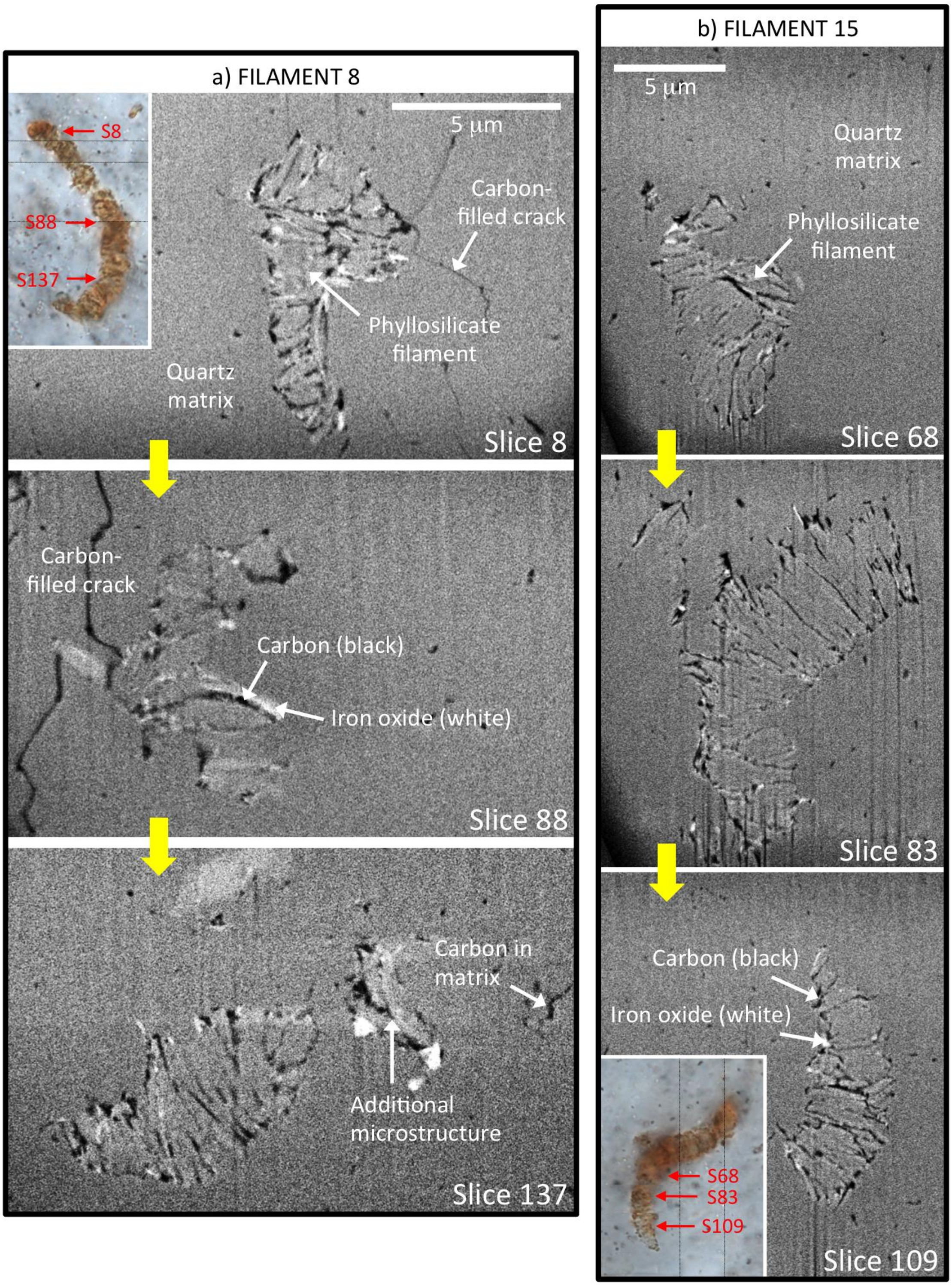
a) FILAMENT 8
S8
S88
S137
5 µm
Carbon-filled crack
Phyllosilicate filament
Quartz matrix
Slice 8
Carbon-filled crack
Carbon (black)
Iron oxide (white)
Slice 88
Carbon in matrix
Additional microstructure
Slice 137
b) FILAMENT 15
5 µm
Quartz matrix
Phyllosilicate filament
Slice 68
Slice 83
Carbon (black)
Iron oxide (white)
S68
S83
S109
Slice 109

Figure 12

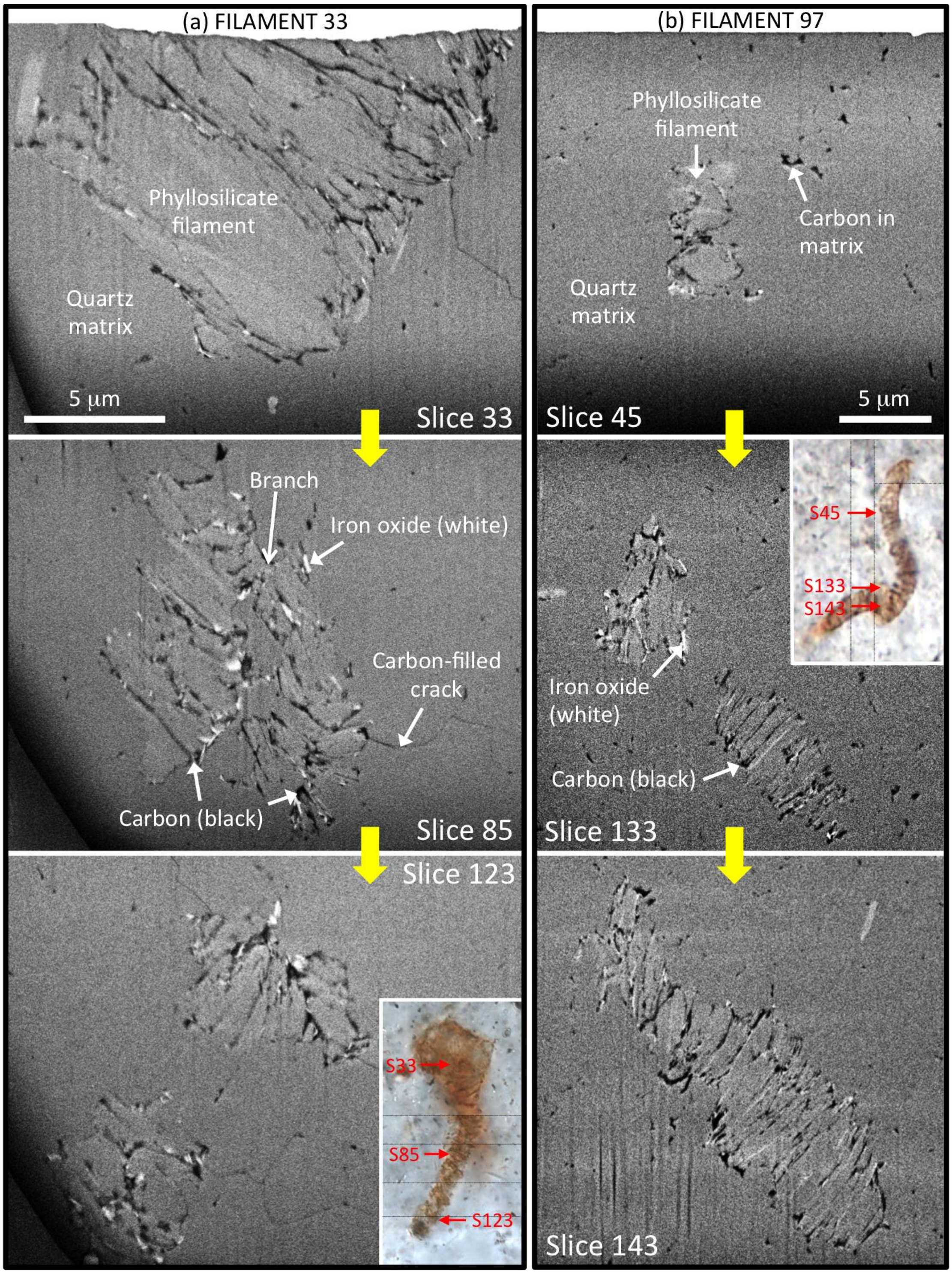
(a) FILAMENT 33
Phyllosilicate filament
Quartz matrix
5 μm
Slice 33
Branch
Iron oxide (white)
Carbon-filled crack
Carbon (black)
Slice 85
Slice 123
S33
S85
S123
(b) FILAMENT 97
Phyllosilicate filament
Carbon in matrix
Quartz matrix
Slice 45
5 μm
S45
S133
S143
Iron oxide (white)
Carbon (black)
Slice 133
Slice 143

Figure 13

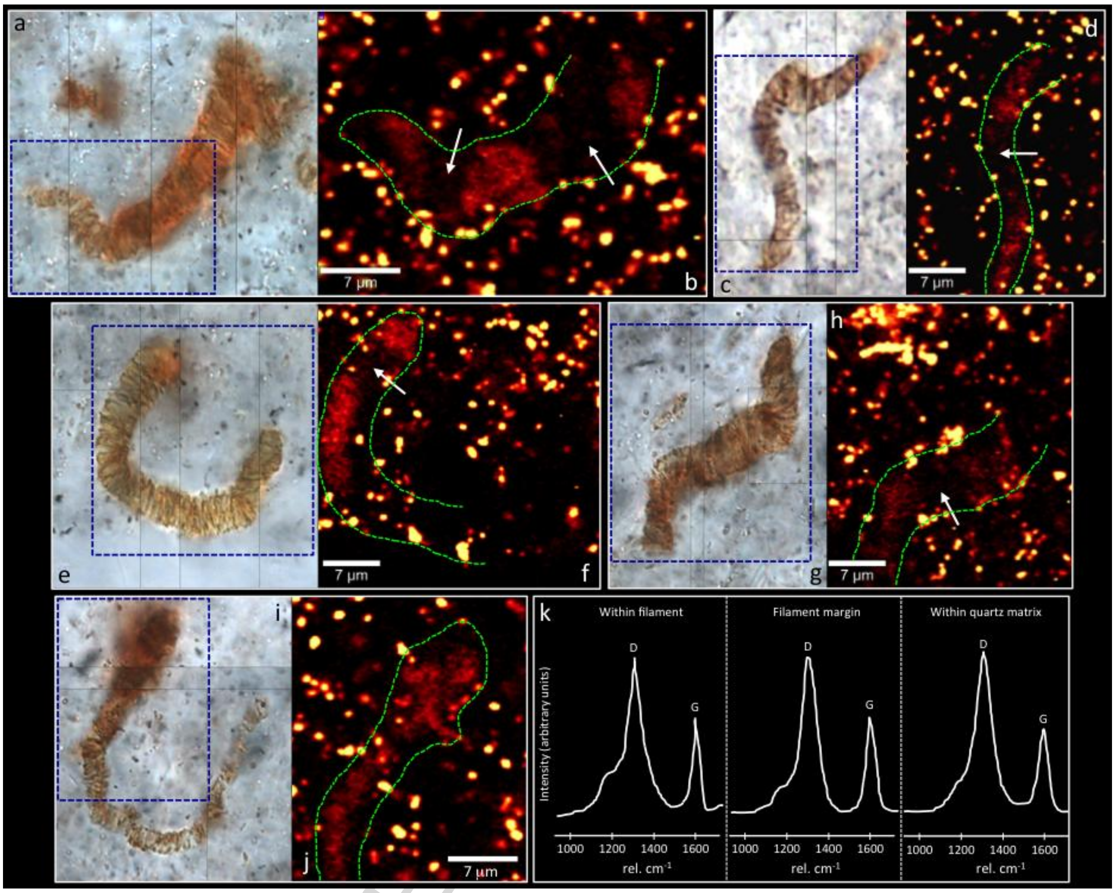
a
b
7 µm
c
d
7 µm
e
f
7 µm
g
h
7 µm
i
j
7 µm
k
Within filament
Filament margin
Within quartz matrix
D
G
Intensity (arbitrary units)
1000 1200 1400 1600
rel. cm-1

Figure 14

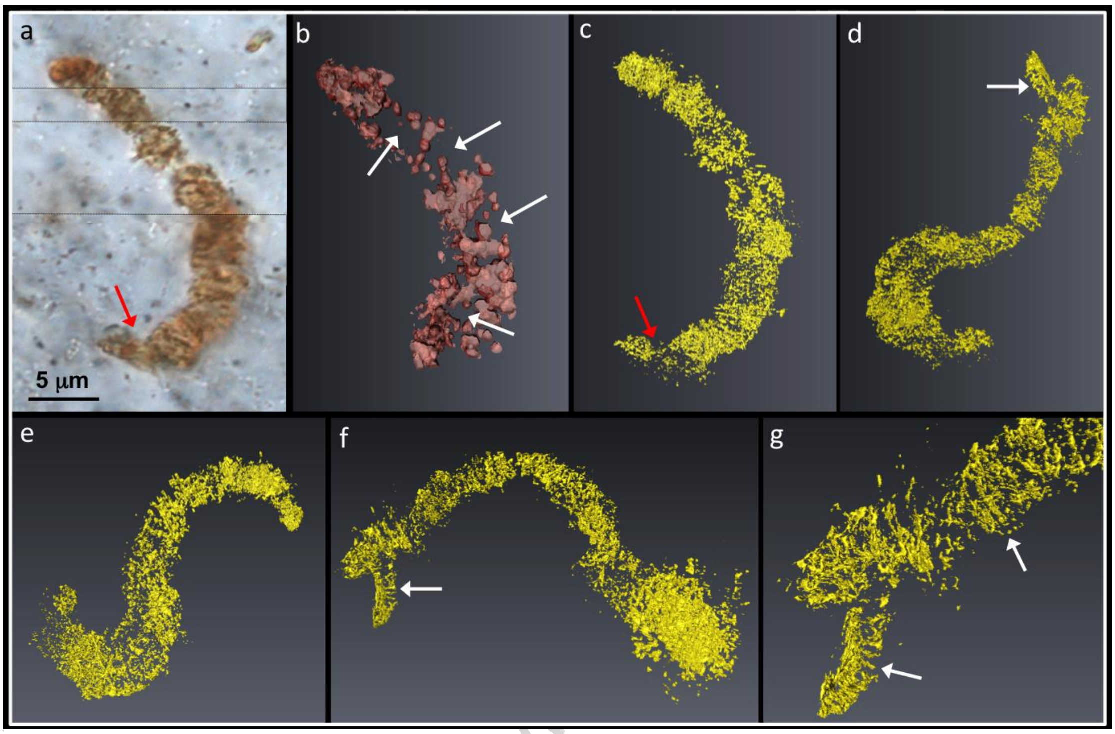

Figure 15

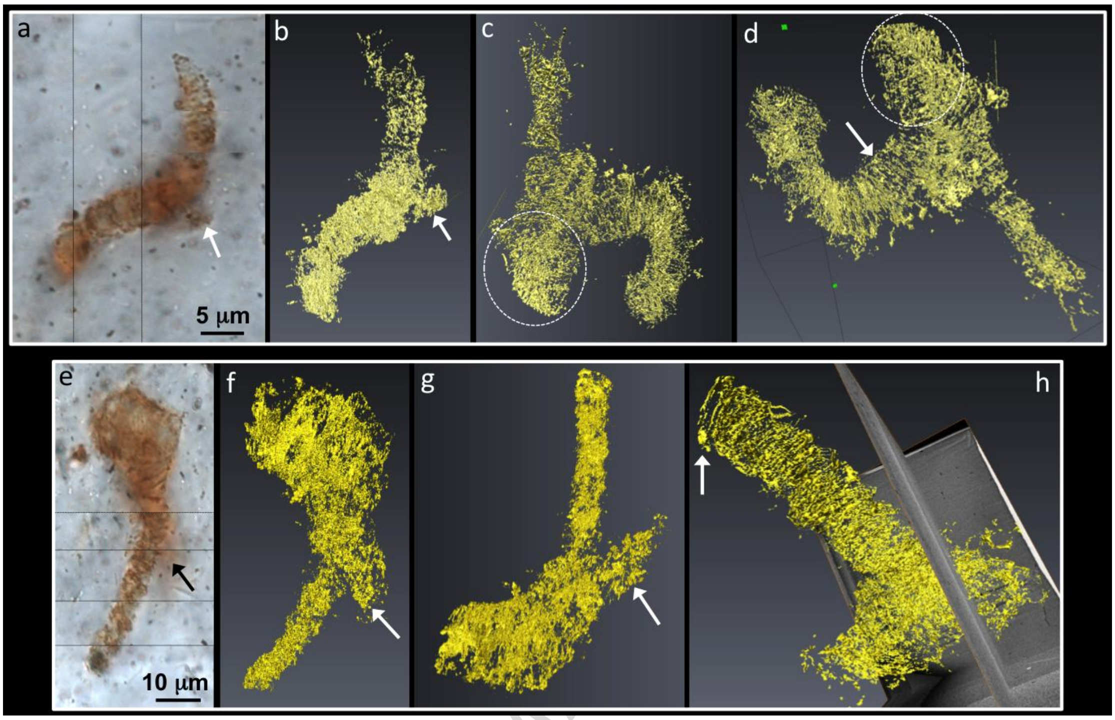

Figure 16

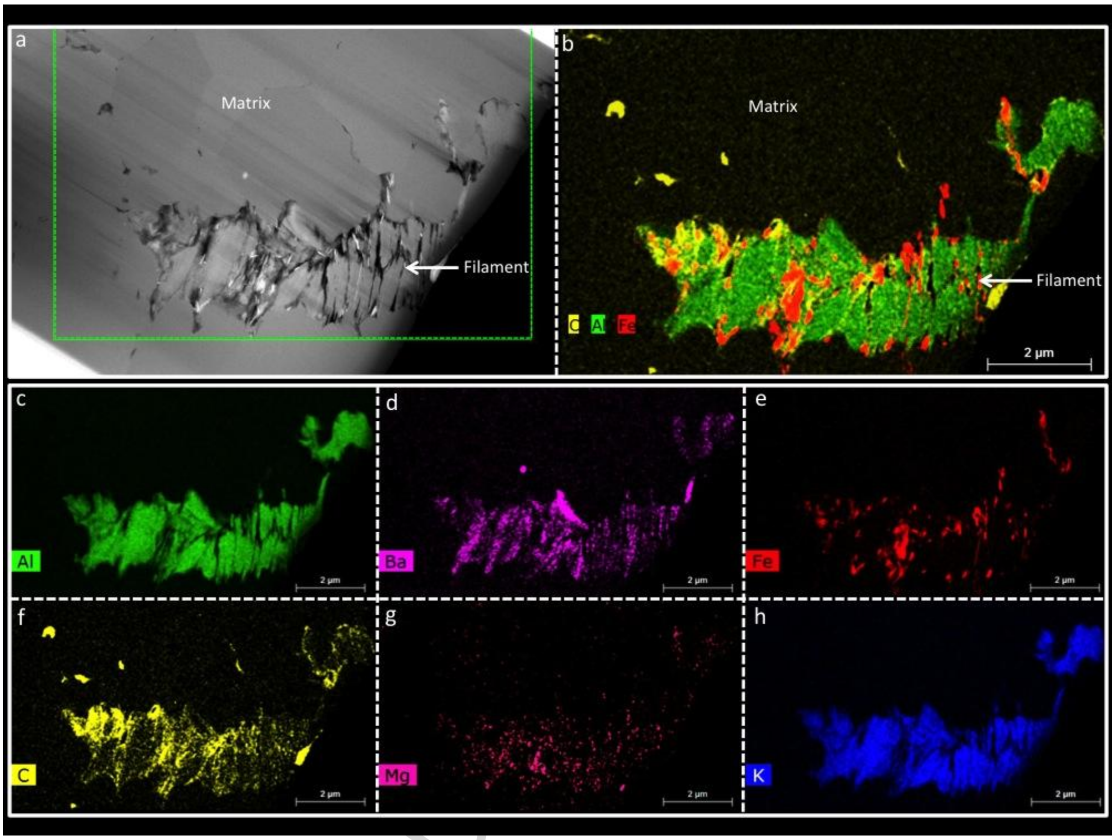

Graphical abstract

Research highlights

- New sub-micrometer analyses of the famous Apex chert ‘microfossils’ are presented
- Candidate filamentous ‘microfossils’ comprise stacks of phyllosilicate grains
- The distribution of carbon is inconsistent with fossilised prokaryote cells
- Carbon also occurs throughout the quartz matrix and in late stage fractures
- ‘Microfossils’ are thus reinterpreted as hydrothermally mediated mineral artefacts